Space Sci Rev (2018) 214:96
https://doi.org/10.1007/s11214-018-0531-4

The Heat Flow and Physical Properties Package (HP^3) for the InSight Mission

T. Spohn[1] · M. Grott[1] · S.E. Smrekar[2] · J. Knollenberg[1] · T.L. Hudson[2] · C. Krause[3] · N. Müller[1] · J. Jänchen[1] · A. Börner[4] · T. Wippermann[5] · O. Krömer[5,6] · R. Lichtenheldt[7] · L. Wisniewski[8] · J. Grygorczuk[8] · M. Fittock[5,9] · S. Rheershemius[5] · T. Spröwitz[5] · E. Kopp[4] · I. Walter[4] · A.C. Plesa[1] · D. Breuer[1] · P. Morgan[10] · W.B. Banerdt[2]

Received: 23 February 2018 / Accepted: 26 July 2018 / Published online: 2 August 2018

Abstract The Heat Flow and Physical Properties Package HP^3 for the InSight mission will attempt the first measurement of the planetary heat flow of Mars. The data will be taken at the InSight landing site in Elysium planitia (136 °E, 5 °N) and the uncertainty of the measurement aimed for shall be better than ± 5 mW m^{-2}. The package consists of a mechanical hammering device called the "Mole" for penetrating into the regolith, an instrumented tether which the Mole pulls into the ground, a fixed radiometer to determine the surface brightness temperature and an electronic box. The Mole and the tether are housed in a support structure before being deployed. The tether is equipped with 14 platinum resistance temperature sensors to measure temperature differences with a 1-σ uncertainty of 6.5 mK. Depth is determined by a tether length measurement device that monitors the amount of tether extracted from the support structure and a tiltmeter that measures the angle of the Mole axis to the local gravity vector. The Mole includes temperature sensors and heaters to measure the regolith thermal conductivity to better than 3.5% (1-σ) using the Mole as a modified line heat

The InSight Mission to Mars II
Edited by William B. Banerdt and Christopher T. Russell

✉ T. Spohn
tilman.spohn@dlr.de

1 DLR Institute of Planetary Research, Rutherfordstr. 2, 12489 Berlin, Germany

2 Jet Propulsion Laboratory, California Institute of Technology, Oak Grove Drive, Pasadena, CA 91109, USA

3 DLR MUSC Space Operations and Astronaut Training, Linder Höhe, 51147 Köln, Germany

4 DLR Institute of Optical Sensor Systems, Rutherfordstr. 2, 12489 Berlin, Germany

5 DLR Institute of Space Systems, Robert-Hooke-Str. 7, 28359 Bremen, Germany

6 Present address: Astrium, Bremen, Germany

7 DLR Institute of System Dynamics and Control, Münchener Strasse 20, 82234 Wessling, Germany

8 Astronika Sp. z o.o., ul. Bartycka 18, 00-716 Warszawa, Poland

9 Present address: OHB, Bremen, Germany

10 Colorado Geological Survey, 1801 19th Street, Golden, CO 80401, USA

source. The Mole is planned to advance at least 3 m—sufficiently deep to reduce errors from daily surface temperature forcings—and up to 5 m into the martian regolith. After landing, HP^3 will be deployed onto the martian surface by a robotic arm after choosing an instrument placement site that minimizes disturbances from shadows caused by the lander and the seismometer. The Mole will then execute hammering cycles, advancing 50 cm into the subsurface at a time, followed by a cooldown period of at least 48 h to allow heat built up during hammering to dissipate. After an equilibrated thermal state has been reached, a thermal conductivity measurement is executed for 24 h. This cycle is repeated until the final depth of 5 m is reached or further progress becomes impossible. The subsequent monitoring phase consists of hourly temperature measurements and lasts until the end of the mission. Model calculations show that the duration of temperature measurement required to sufficiently reduce the error introduced by annual surface temperature forcings is 0.6 martian years for a final depth of 3 m and 0.1 martian years for the target depth of 5 m.

Keywords Mars · Heat flow · Regolith · Thermal conductivity · Temperature gradient · Surface temperature · Radiometer · Thermal inertia

1 Introduction

1.1 Scientific Objectives

Planets in general and terrestrial planets such as Mars in particular can be regarded as engines that convert heat into mechanical work (geology) and magnetic field energy (e.g., Spohn 2015). Heat was stored in their interiors during accretion and differentiation early on and has been generated by the decay of the long-lived radiogenic isotopes of U, Th and K ever since. Heat is transferred to the surface of terrestrial planets by conduction through the lithosphere including the crust where it can be measured as the surface heat flow. Measuring the surface heat flow of Mars is the main task of the Heat Flow and Physical Properties Package (HP^3) onboard the InSight mission. The instrument described in the present paper measures the surface temperature and the temperature gradient as well as the thermal conductivity in the topmost 5 m of the Martian regolith. The surface heat flow is calculated from the temperature gradient and the thermal conductivity. The rate of advance of the probe to depth places constraints on the mechanical properties of the regolith.

While thermal conduction through the lithosphere characterizes regions lacking tectonism and volcanism, heat transport by convection dominates in the sub-lithospheric mantle and possibly in the core. Convection is the mechanism by which heat can be converted into mechanical work and is fundamental to dynamo mechanisms that generate magnetic fields in planetary cores. The heat flow from the interior of a planet is indicative of the rates of internal heat and mass transfer but also of the concentration of radiogenic elements and thus the composition of the planet. Numerical modeling of heat transfer in planetary interiors suggests that the rate of heat production can be estimated from the surface heat flow. Plesa et al. (2015) find the ratio between the integrated interior heat production rate and the surface heat flow—termed the bulk Urey ratio—to likely be 0.6 for present Mars. Comparison with published Urey ratios for Earth must be considered carefully as these are often mantle Urey ratios (ratio between heat flow from the mantle and the mantle heat production rate) that tend to be smaller than bulk planet Urey ratios. Estimates for the Earth bulk Urey ratio range mostly from 0.3 to 0.5 (see Jaupart and Mareschal 2015 for a recent review). Heat

piping through volcanism, for instance, (e.g., Breuer and Spohn 1993; Nakagawa and Tackley 2012) may be causing a smaller bulk Urey ratio for Earth, which is significantly more volcanically active than Mars at present.

Estimates of the martian surface heat flow in the literature vary. Most are based on cooling models using parameterized convection schemes and compositional models (e.g., Stevenson et al. 1983; Spohn et al. 2001; Hauck and Phillips 2002; Fraeman and Korenaga 2010; Grott et al. 2010; Morschhauser et al. 2011) or fully dynamical convection schemes (e.g., Kiefer and Li 2009; Plesa et al. 2015, 2016a). Others use estimates of the thickness of the lithosphere, its basal temperature and thermal conductivity (e.g., McGovern et al. 2002, 2004; Grott et al. 2005, 2007; Ruiz et al. 2009; Phillips et al. 2008). All these models are rather crude estimates, using reasonable albeit not directly measured quantities. In any case, the estimates suggest the martian present day surface heat flow to be around 20–30 mW m^{-2}, for some geochemical models (Lodders and Fegley 1997) even 50 mW m^{-2}. A simple comparison with the Earth average surface heat flow of 95 mW m^{-2} (e.g., Jaupart and Mareschal 2015) confirms an estimate of roughly 35 mW m^{-2} observing that for the same composition the surface heat flow should scale with the radius of the planet times its average density.

For present-day Mars, tidal dissipation and dynamo action are negligible as sources and sinks of heat. As a comparatively small planet without operating plate tectonics, Mars is believed to have cooled by thickening of its massive lithosphere and convective vigour in the mantle is believed to have decreased compared to earlier epochs such as the Noachian when the planet was much more volcanically active (e.g., Greeley and Spudis 1981; Spohn et al. 1998). Thermal evolution models suggest that the surface heat flow should have decreased with the convective vigour but also because the radiogenic heat production rate decreases with time (e.g., Breuer and Moore 2015) by roughly a factor of 1.5 to 2 since the Noachian.

Surface heat flow varies between geological provinces on Earth. For example, at mid-oceanic ridges, where upwelling mantle flow reaches the surface, heat flow is up to several 100 mW m^{-2} while on continental shields, where a thick lithosphere covers the convecting mantle, a few 10 s of mW m^{-2} are observed (see Jaupart and Mareschal 2015 for a recent review). In addition to the mantle contribution, the variation of the surface heat flow is a strong function of the variation of the thickness of the crust and lithosphere. The variation with the lithosphere thickness has been used to estimate paleo-heat flow values on Mars (e.g., Schultz and Watters 2001; McGovern et al. 2002, 2004; Grott et al. 2005; Kronberg et al. 2007; Ruiz et al. 2009; Hauber et al. 2010). The crust is generally understood as being a product of partial melting of the mantle. Heat producing elements, because of their valence states and large ionic radii, tend to be enriched in partial melt and therefore crustal rock is enriched as compared with mantle rock (e.g., Taylor 2008; Hofmann 2014), likely forming a dominating contribution to the surface heat flow. On a planet like Mars where the convecting mantle is covered by a thick lithosphere, variations in surface heat flow may largely reflect variations in crustal thickness as has been suggested by e.g., Plesa et al. (2016a). SEIS (Lognonné et al. 2018) will measure the crustal thickness to within $\pm$10 km, whereas at present the uncertainty is a factor of two, at least.

Unfortunately, the heat flow from the interior of a terrestrial planet is small in comparison with the solar flux, and surface temperature variations are mostly caused by variations in insolation and atmospheric heat transfer. Therefore, the surface heat flow cannot be measured directly as infrared luminosity as has been done for giant planets (e.g., Guillot and Gautier 2015) or for Io (e.g., Spencer et al. 2000). Rather, the surface heat flow is calculated from a measurement of the near surface temperature gradient and the regolith thermal conductivity (Bullard 1939, 1954, see also Hagermann 2005 and Jaupart and Mareschal 2015 for reviews) taking the tacit assumption that the surface heat flow is in equilibrium with the heat

flow from the deeper interior. In general, the temperature gradient needs to be measured at a depth where perturbations caused by variations in solar insolation and atmospheric disturbances are sufficiently small. Other disturbances may be due to past climate change (Mellon and Jakosky 1992) caused by e.g., obliquity variations (Laskar et al. 2004) but these should be sufficiently small at the InSight landing site near the equator. However, it is worth noting that for the mid and upper latitudes, climate induced signals can actually dominate the surface heat flow. Moreover, regional context needs to be considered (Siegler and Smrekar 2014). In any case, no near surface temperature gradient and thermal conductivity data have hitherto been taken at Mars and the InSight mission will be the first to attempt to measure its surface heat flow.

In the absence of direct measurements, martian heat flow has been estimated from the deformation of the lithosphere under mechanical loads (e.g., Schultz and Watters 2001; McGovern et al. 2004; Grott et al. 2005; Ruiz et al. 2009; Phillips et al. 2008), yet large uncertainties are associated with this method. Interpretation of the obtained heat flow estimates is further complicated by the fact that the time of load emplacement does not necessarily represent the time the lithospheric shape was frozen-in, as lithospheric deformation will usually continue after loading is finished. This is due to lithospheric stress relaxation by creep (Albert and Phillips 2000), a process particularly important for multi-layer rheologies (Brown and Phillips 2000). Further, the crater retention age of the corresponding surfaces may not represent the time of deformation (Beuthe et al. 2012), as they may have been overprinted by later activity.

Therefore, direct heat flow measurements are needed to constrain the thermal state of Mars (e.g., Grott et al. 2007; Dehant et al. 2012). Without plate tectonics, Mars can be considered geophysically less complex than the Earth and average surface heat flow on Mars can likely be constrained from measurements at only a few well chosen sites (Plesa et al. 2016a). Terrestrial heat flow is also affected by hydrothermal circulation which has not operated on Mars for billions of years. Surface heat flow variations on Mars are expected to be mostly driven by differences in crustal thickness as well as by the distribution of heat producing elements and this contribution (Hahn et al. 2011) can be estimated from models of crustal thickness (Zuber et al. 2000; Neumann et al. 2004; Wieczorek and Zuber 2004) as well as gamma ray spectroscopy data (Taylor et al. 2006a,b). Mantle dynamics should play a smaller role as far as variations in regional heat flow are concerned (Grott et al. 2010; Plesa et al. 2016a) except perhaps for major plumes such as possibly underneath Tharsis and Elysium. Even a single measurement will serve as an important anchoring point for models of the martian thermal evolution, and global estimates can be obtained by extrapolating the local measurement using complementary global data-sets.

One example for a model of the present-day heat flow is shown in Fig. 1 (see Plesa et al. 2015, 2016a for a more detailed discussion), where surface heat flow is shown as a function of geographical location. The map has been calculated from a model of the thermal evolution of Mars from after core formation to the present using a 3D mantle convection code. Estimates of crustal thickness (Neumann et al. 2004), the distribution of heat producing elements (Taylor et al. 2006a), as well as their bulk abundance (Wänke and Dreibus 1994) served as model input. The convection model takes a temperature and pressure dependent viscosity as well as pole-to-equator surface temperature variations into account. As shown in Fig. 1, surface heat flow varies between 17 and 37 $\mathrm{mW\,m^{-2}}$ between the Hellas basin and the Tharsis province, respectively, and variations generally follow the trend imposed by the assumed crustal thickness, while mantle upwellings play a minor role. Note that the predicted areas of highest heat flow near Tharsis and Elysium coincide with areas for which volcanic resurfacing has been fairly recent (Neukum et al. 2004; Hauber et al. 2011; Vaucher et al. 2009a,b).

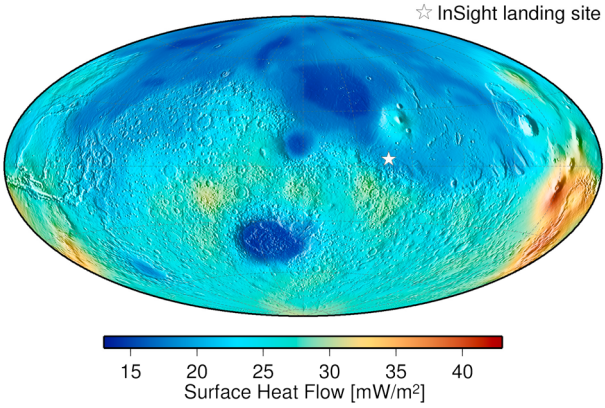

Fig. 1 Color coded map of the present-day surface heat flow on Mars as predicted by 3D thermal evolution models (Plesa et al. 2015, 2016a). A bulk concentration of heat producing elements following Wänke and Dreibus (1994) has been assumed. It is further assumed that the crust is enriched in heat producing elements by a factor of 10 as suggested by gamma ray data (Taylor 2008). The crust thickness model has been adopted from Wieczorek and Zuber (2004) and is based on recent gravity and topography data. A detailed description of the model and parameter values can be found in Plesa et al. (2016a). The asterisk marks the planned InSight landing site

Plesa et al. (2015, 2016a) have calculated average surface heat flow values for Mars using various models of the planet's bulk composition and concluded that some of the compositional models might be distinguishable if the globally averaged surface heat flow of Mars were known. While the models of Treiman et al. (1986) and Wänke and Dreibus (1994) give similar values of average surface heat flow between 22.5 and 26.6 mW m^{-2} and cannot be distinguished from each other, the model by Lodders and Fegley (1997) implies an average heat flow about twice as large. For the model of Morgan and Anders (1979), an average surface heat flow of about 30 mW m^{-2} is calculated. However, this model has a higher Th than K abundance, which is inconsistent with the elemental abundance ratios obtained for the martian meteorites and the crustal abundances measured from orbit (Taylor et al. 2006a,b). Even with a single point measurement, considering the predicted variation of the heat flow between these models and across the surface, HP^3 should help to narrow the uncertainties in the composition of Mars.

1.2 Brief Description of the Instrument and Outline of the Paper

The basic components of the Heat Flow and Physical Properties Package are shown in Fig. 2. HP^3 will use the Mole, a self-impelling, slow penetrator of about 400 mm length and 27 mm diameter to carry the Science Tether, a tether equipped with 14 platinum resistance temperature sensors (PT100) to a target depth of at least 3 m and up to 5 m. The instrumented science tether is termed TEM-P (for Thermal Excitation and Measurement-Passive), for brevity. The temperature measurement will be complemented by measurements of the thermal conductivity using a modified line heat source method at 50 cm intervals as the Mole advances into the subsurface. This will be accomplished by heating foils (TEM-A, short for Thermal Excitation and Measurement-Active) integrated in the Mole outer hull that are served with a constant power and will measure the temperature increase upon heating. The latter is a measure of the heat conducted to the surrounding regolith and thus of its thermal conductivity.

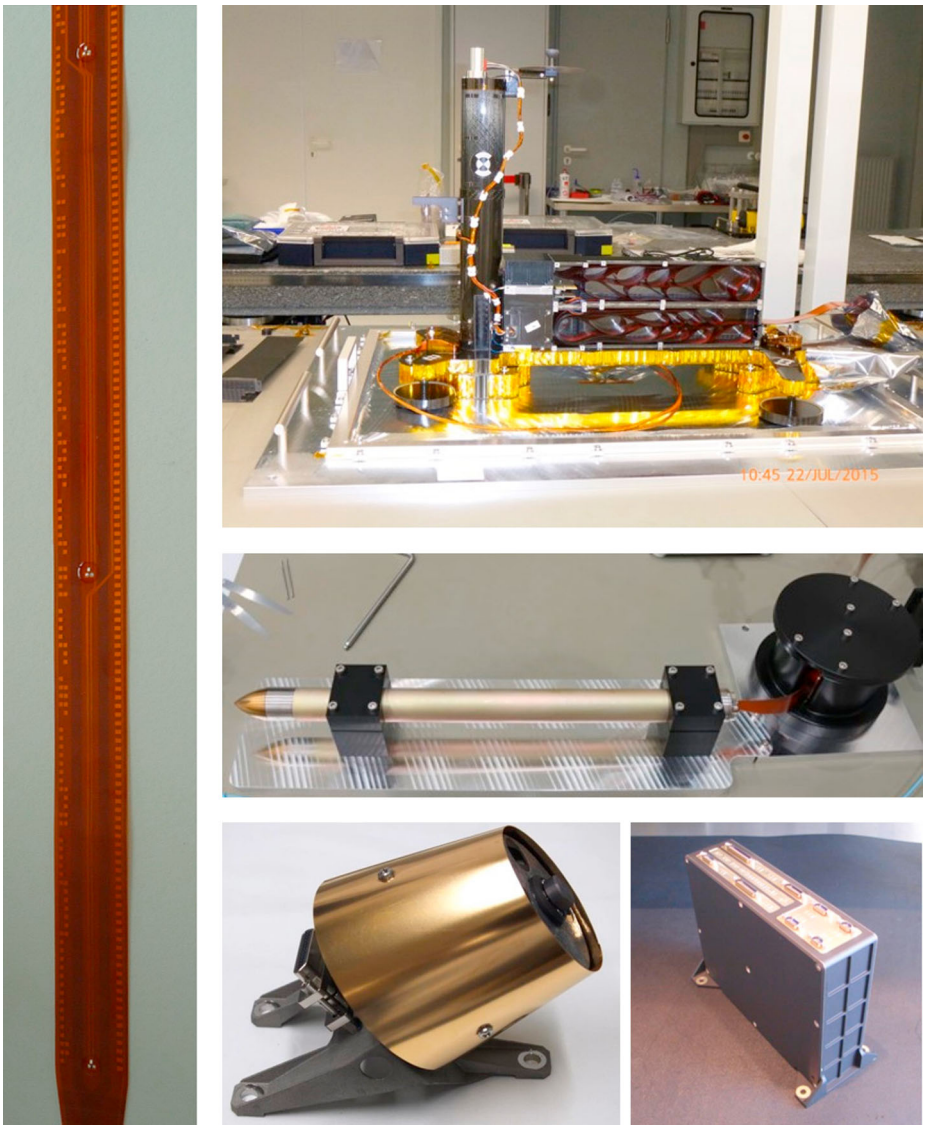

Fig. 2 Elements of the Heat Flow and Physical Properties Package (HP^3) flight model. Top right: Support Structure Assembly (SSA) with the cover of the tether compartment removed. The science tether is stored in the upper compartment, the engineering tether in the lower. The Mole is stored vertically in the center of the tube, the Mole launch lock is visible at its top. The grappling hook used for deployment of the SSA onto the martian surface is also attached to the top of the tube. Middle right: Mole and science tether mounted to the support equipment used for transport. The Mole length is 400 mm from the tip to the end of the backcap. Left: Section of the science tether TEM-P close to the Mole facing end showing the absolute and relative depth encoding on its left and right edge, respectively. The distance of the three (of 14) temperature sensors visible from the tip of the Mole is 497, 727, and 977 mm (from bottom to top), respectively. Bottom middle: The HP^3 radiometer. Bottom right: The HP3 back end electronics box, which is mounted inside the lander's warm electronics box

The path of the mole will be traced using TLM (short for Tether Length Measurement device) which measures the length of tether paid-out and STATIL (short for STAtic TIltmeter) which measures the attitude of the mole. Before being deployed, the Mole and the tether will be housed in the Support Structure Assembly (SSA) which also houses the TLM. The package further includes a radiometer (RAD) mounted on the lander to measure the surface brightness temperature. The package will be commanded and data will be handled through a backend electronics (BEE) box housed within the warm electronics box on the lander. The BEE will be connected to the SSA by the so-called engineering tether. Before deployment, the latter is stored in the SSA as well.

The requirements for the sensors, depth of measurement and its duration will be discussed in detail in the following Sect. 2. The hardware will be described in detail in Sect. 3. The heat flow error budget will be discussed in Sect. 4 and the instrument operations in Sect. 5.

2 Surface Heat Flow, Regolith and Measurement Requirements

2.1 Measuring the Planetary Surface Heat Flow

In order to determine the heat flow to the uncertainty required by the mission science goals of ± 5 mW m^{-2} surface thermal perturbations must be avoided as much as possible. On Earth's continents, measurements are usually taken in boreholes that are tens to hundreds of meters deep (Pollack et al. 1993), as the shallow subsurface temperatures are dominated by seasonal temperature changes. The situation is different for the oceanic lithosphere, as the close-to-constant water temperature at depth allows for measurements to be taken in the upper 5 m of seafloor sediment (Bullard 1954). The technical difficulties associated with drilling boreholes of sufficient depths on planets other than the Earth have so far only been overcome during the Apollo program, and successful heat flow measurements have been performed during the Apollo 15 and 17 missions. The astronauts emplaced sensors to depths of 1.38 m and 2.34 m at the Apollo 15 and 17 sites (Langseth et al. 1972, 1976), respectively. The Apollo 16 probe also reached >2 m depth, but the read-out tether was damaged and no measurements could be taken. Measurements with such comparatively shallow depth are feasible because of the low thermal conductivity of the lunar regolith that prevents surface temperature perturbations to propagate to larger depths.

Heat flow measurements on Mars are expected to be more challenging than on the Moon: First, boreholes on Mars need to be deeper than on the Moon due to the larger expected thermal conductivity on Mars. Though thin, the martian atmosphere within regolith pore spaces considerably increases its conductivity compared to the regolith on an atmosphereless body (e.g., Hütter et al. 2008; Piqueux and Christensen 2009a,b). Cements in the regolith (Piqueux and Christensen 2009b) and aeolian sorting of regolith particle sizes may increase interparticle contact and make the martian regolith more conductive to heat. Martian regolith thermal conductivity is therefore expected to be larger than lunar values by a factor of two to five (e.g., Grott et al. 2010), requiring measurements on Mars to be both deeper and of longer duration to achieve the required level of uncertainty.

Another difference between the upcoming martian heat flow measurement and the Apollo experiments is the way the probe will be deployed: While the Apollo astronauts used handheld rotary percussion drill systems to emplace the probes away from surface perturbations (Langseth et al. 1972; Heiken et al. 1991), the HP^3 instrument will be placed onto the surface by a robotic arm with limited reach. Therefore, perturbations caused by the landing system

and the lander itself need to be taken into account during data analysis (Grott 2009; Kiefer 2012). One of these perturbations is the blowing-away of surface dust during landing, as has been observed for the Phoenix and Curiosity landing sites (Daubar et al. 2015). The dust removal may result in albedo changes and that, in turn, may change the heat balance. Timescales for dust resettling have been estimated from HIRISE data as well as the re-brightening of rover tracks (Geissler et al. 2010), and resettling can take up to a martian year or longer. Aeolian sediment transport seems to be the dominant process for re-brightening (Geissler et al. 2010), while fallout of dust from the atmosphere seems to play only a minor role.

Another source of thermal perturbations is the lander itself, which casts shadows during daytime and acts as a radiator during the night. In total, the lander is estimated to change the average surface temperature by up to 4 K in the vicinity of the lander (Siegler et al. 2017), and lander induced perturbations can thus have a significant influence on the surface energy balance. Care must be taken to remove these contributions during data analysis, and the HP^3 radiometer will be used to determine the surface brightness temperature variation over the duration of the mission and thus the surface boundary condition for modeling the subsurface data.

Dust loading of the martian atmosphere is a potential additional source of perturbation that may affect the surface heat flow measurement. Models using dust opacity data obtained by the Mars Exploration Rover Opportunity (Lemmon et al. 2015), however, indicate that the subsurface heat flow only moderately varies following a global dust storm and that the perturbations are less than 2.5 mW m^{-2} at depths below 3 m for a thermal conductivity of 0.05 W m^{-1} K^{-1}. Regional dust storms, which are of shorter duration and smaller magnitude introduce even considerably smaller perturbations (Plesa et al. 2016b).

Finally, the martian spin axis lacks stabilization due to the absence of a large moon, and chaotic obliquity changes have been predicted from dynamical simulations (Laskar et al. 2004). These calculations are supported by geological evidence that suggests climate changes on timescales of a few million years (Mustard et al. 2001; Kreslavsky and Head 2002; Head et al. 2003; Helbert et al. 2005). However, it has been shown that such long term signals have only a small effect on the subsurface thermal gradient (Grott et al. 2007), especially if an equatorial landing site is chosen (Mellon and Jakosky 1992). Recently, Lorenz (2015) estimated the influence of a sunspot driven change in insolation on subsurface temperatures, concluding that the signal might be detectable in the InSight data.

2.2 Mars Surface and Regolith Properties at the InSight Landing Site

The physical properties of the regolith at the landing site are of utmost importance to the success of the HP^3 experiment. The rate of advancement of the Mole and the final depth reached depend on the soil mechanical properties (e.g., Lichtenheldt et al. 2014; Seweryn et al. 2014). The uncertainty of the heat flow measurement will depend on the thermal properties of the regolith (e.g., Grott et al. 2010). Unfortunately, these values are not well known for Mars in general and not for the InSight landing site. What is known about the regolith has been reviewed in detail with a specific focus on the needs of the InSight mission by Golombek et al. (2017) and by Morgan et al. (2018). In this section, we will restrict ourselves to a short compilation of the most relevant parameter values.

High resolution images of the landing site from the HIRISE camera on the Mars Reconnaissance Orbiter (MRO) and thermal emission spectral data at various wavelengths from the Viking Thermal Mapper and the Thermal Emission Spectrometer TES on Mars Global Surveyor (MGS) have been used to estimate the surface and regolith properties of the landing

site, such as rock abundance. The landing ellipse has very low rock abundance (Golombek et al. 2017) of only a few percent (fractional area covered by high-thermal inertia rock), an important observation for Mole success. Aeolian processes such as those causing desert pavement on Earth (e.g., Golombek et al. 2006) and granular convection (e.g., the Brazil-nut effect (e.g., Güttler et al. 2013)) induced by impacts or seismic shaking may cause the rock abundance to decrease with depth. Most rocks at the landing site are concentrated around rocky ejecta craters larger than 30-200 m in diameter (Golombek et al. 2013, 2017) where the rock abundance can reach up to 35%. The crater size and ejecta observations have been used to estimate and map the thickness of the regolith giving depths to the underlying competent layer of between 3 and 17 m (e.g., Warner et al. 2017). The competent layer is likely strong intact basalt (Golombek et al. 2013, 2017). If the Mole encounters a rock larger than a few 10s of cm as it moves forward, it could be blocked from further advancement. The likelihood of such an encounter between the surface and the required (3 m) or target (5 m) depths has been calculated to be 43% and 59%, respectively. This estimate uses the most pessimistic models, where the surface rock abundance is taken as 5% and the Mole is stopped by any rock regardless of shape or orientation if it is 10 cm or larger. If less conservative assumptions are made about surface rock abundance (e.g., 2.5% or less) and demonstrated capabilities of the Mole are allowed for (e.g., the Mole can push rocks up to 15 cm out of its way within the regolith, and can also deflect around rocks encountered at angles $\leq$45 degrees), the probability of success increases to 98% and 90%, respectively (Golombek et al. 2017).

The thermophysical properties of the landing site also suggest that the regolith that makes up the surface material is conducive to emplacing the heat flow probe (Golombek et al. 2017), where low-cohesion, moderate to poorly-sorted and sand-sized grains are among the most favorable for Mole movement. The thermal inertia ranges from 130 to 220 with a median value of 180 $\mathrm{J\,m^{-2}\,K^{-1}\,s^{-1/2}}$, the albedo is 0.25, and dust cover index is 0.94 (Golombek et al. 2017). Comparison with the thermal inertias of existing landing sites and the regolith present (Golombek et al. 2008) suggests that the InSight landing site regolith is composed of cohesionless or low cohesion sand (cohesions of less than a few kPa, angle of internal friction of 30–40°), with bulk density of $\sim$1000–1600 $\mathrm{kg\,m^{-3}}$, particle sizes of $\sim$150–250 μm (fine sand), that extends to a depth of at least several tens of centimeters, and with surficial dust (of low abundance) less than 1–2 μm (Golombek et al. 2017). Tests with Quartz sand at DLR Bremen have shown that the Mole can advance to 5 m depth in such sands within less than 10 hours.

With the above estimates of a representative thermal inertia and a near surface density times heat capacity of 8×10^5 $\mathrm{J\,m^{-3}}$ (Morgan et al. 2018), the thermal conductivity at the surface can be estimated to be 0.017 to 0.048 $\mathrm{W\,m^{-1}\,K^{-1}}$. Using relationships established in the laboratory (Presley and Christensen 1997; Presley and Craddock 2006), the thermal conductivity is likely dominated by that of the CO_2 gas contained in the regolith. The latter varies primarily with gas pressure and particle size, and to a lesser extent with temperature. Pressure and particle size dependence has been empirically constrained by Presley and Christensen (1997), Presley and Craddock (2006) and is given by

$$k(P) = C\,P^{0.6} d^{-0.11\log(P/K)} \tag{1}$$

where $C = 5.0 \times 10^{-3}$ and $K = 1.08 \times 10^4$ kPa are empirical constants, d is the grain diameter in μm, and P the (atmospheric) pressure in kPa (compare also Piqueux and Christensen (2009a,b)). The variation of the gas contribution with temperature follows a square root dependence but the total temperature dependence is negligible for the temperature range considered here (Morgan et al. 2018). It is, of course, reasonable to assume that the thermal

conductivity will be affected by stress anisotropy and that the passage or the presence of the Mole would disturb the stress distribution upon advancement in the regolith. As Morgan et al. (2018) discuss, the latter effects are likely to be too small to seriously affect the uncertainty of the measurement.

The surface thermal emissivity of martian soil has been estimated *in situ* using the mini-TES instrument on the two Mars Exploration Rovers Spirit and Opportunity (Ruff et al. 2006). Morgan et al. (2018) conclude that an emissivity value of 0.98 (+1%/−2%) should be representative of the surface material at the InSight landing site.

2.3 Measurement Requirements

The Level 1 science objective of the HP^3 experiment is a determination of the surface heat flow F at the landing site with an uncertainty of better than ± 5 mW m^{-2}. Heat flow, or to be more precise the heat flux density, is given by

$$F(z) = k(z)\frac{dT}{dz} \tag{2}$$

where z is depth, $k(z)$ is the depth-dependent regolith thermal conductivity, and T is temperature. Therefore, the local thermal conductivity as well as the local thermal gradient must be determined.

Diurnal, annual, and interannual surface temperature variations cause perturbations of the temperature field in the regolith. The depth to which these perturbations propagate measurably may be estimated by calculating the skin depth d_ϵ at which the surface signal has decreased by a factor of $1/e$ (e.g., Beardsmore and Cull 2001)

$$d_\epsilon = \sqrt{\frac{\kappa \Pi}{\pi}} \tag{3}$$

where κ is the regolith thermal diffusivity and Π is the period of the perturbation. Given conservative bounds of regolith thermal conductivity between 0.01 and 0.1 W m^{-1} K^{-1} and regolith density and heat capacity (8×10^5 J m^{-3}) as discussed by Morgan et al. (2018), worst case skin depths of 0.04 and 1.4 m result for diurnal and annual periods, respectively. While the HP^3 thermal sensors can easily be placed below the reach of the diurnal temperature wave, penetrating more than a few annual-wave skin depths is not feasible for the Mole and instrumented tether. Thus it is expected that the surface driven perturbations (decreasing in amplitude with depth) will be superimposed on the planetary heat flow measurements. In order to remove the disturbance, measurements need to be carried out over an extended period of time (Grott et al. 2007), preferably spanning the range of a full martian year, although a shorter timespan is permissible. In Sect. 4 we will show that 0.1 martian year will suffice if the Mole tip achieves a depth of 5 m while a tip-depth of 3 m will require 0.6 martian years of data. The estimate will depend on the (yet unknown) value of the regolith thermal conductivity. This estimate assumes a nominal value of 0.05 W m^{-1} K^{-1} for this estimate. Given the mission profile, HP^3 is required to reach a minimum depth of 3 m. At this depth, we will be safely underneath the diurnal thermal wave and be capable of correcting for the disturbance by the annual wave.

To have some margin with respect to present-day models, derivation of HP^3 measurement requirements is based on expected surface heat flows between 10 and 50 mW^{-2}, which for the desired uncertainty of ± 5 mW m^{-2} corresponds to a measurement uncertainty of 50% to 10%, respectively. Assuming the measurement uncertainties for thermal conductivity and

thermal gradient to be independent and normally distributed, Gaussian error propagation can be employed to derive error budgets of 7% for each of the two measurements (compare Sect. 4).

The main contributors to the thermal gradient error budget are the measurement uncertainties of temperature differences among sensors and the precise depths of those sensors. Again assuming independent and normally distributed errors, each of these measurements is allowed an uncertainty of 5%. In the worst case of low heat flow (10 mW m^{-2}) and high thermal conductivity (0.1 W m^{-1} K^{-1}), a temperature difference of 0.2 K needs to be resolved over a 2 m baselength.

The method for determining thermal conductivity in a thermally isotropic medium relies on injecting a specified amount of heat into the ground and measuring the sensors self-heating curve (see Sect. 3.4). While analytical solutions exist to predict self-heating curves for sensors with a very large to moderate length to diameter ratio (Jaeger 1956; Carslaw and Jaeger 1959; Nagihara et al. 2014), numerical methods (Grott et al. 2010) are foreseen to be applied for HP^3, which uses the Mole as a modified line heat source. Major contributors to the thermal conductivity error budget are the uncertainties of the temperature rise and uncertainties in the thermal model used to calculate the TEM-A self heating curve. The TEM-A heating curve has been calibrated using the best available reference materials, which leaves an uncertainty of 2.5% at a 1-σ level (Hammerschmidt and Sabuga 2000a,b), however.

The main purpose of the HP^3 radiometer (RAD) is the determination of the shape of the surface temperature forcing, which acts as the boundary condition for the measured subsurface temperatures. In this regard, absolute temperatures are of secondary importance, although they will be used to constrain surface thermal inertia. RAD will measure the surface brightness temperature of the martian regolith inside its field of view, but in order to link these measurements to those in the subsurface, the kinetic surface temperature needs to be estimated. This in turn is linked to the brightness temperature through the regolith's emissivity, and the Mars Exploration Rovers provided data of surface emissivity from mini-TES data. Surface emissivity from various targets on the two explored regions in Gusev Crater and Meridianum Planum analyzed by (Ruff et al. 2006) indicate that the effective surface emissivity in the 8–14 μm band is likely in the range from 0.95 to 0.99 (Morgan et al. 2018), consistent with assumptions in previous work (Mellon et al. 2000; Helbert et al. 2006). As surface dust on Mars consists largely of aeolian sediment and forms a global unit (Yen et al. 2005), emissivity of the dust can be expected to be similar in all regions of the planet. Modeling of the RAD instrument performance indicates that a random measurement error equivalent to 4 K at 150 K brightness temperature is less significant than the possible error from the unknown emissivity for estimating the kinetic surface temperature, and 4 K is thus used as the measurement requirement for the RAD surface brightness determination.

3 Instrument Design

3.1 Design Overview

The most fundamental quantities to be measured by the Heat Flow and Physical Properties Package (HP^3) are the thermal conductivity of the regolith and its variation with depth and the temperature as a function of depth in the topmost 5 m of Mars. In addition, the surface brightness temperature will be determined using the HP^3 radiometer (RAD). To measure the subsurface temperature and thermal conductivity, a self-hammering Mole will carry a suite of temperature sensors and heaters (the TEM sensor suite TEM-A and TEM-P) to depth.

The advancement of the Mole is monitored with the tether length monitor (TLM) and with the static tiltmeter (STATIL). The path of the Mole and the sensor-embedded tether can be reconstructed by combining data from TLM, which measures the amount of tether paid out, and STATIL, which determines the orientation of the Mole axis with respect to local gravity. In summary, the instrument package consists of the following functional sub-units (Fig. 2).

1. Support Structure Assembly (SSA) with TLM, the Science Tether TEM-P, and the Mole. The SSA also includes the tether connecting the Back End Electronics (BEE) and the deck harness with the SSA.
2. Mole (including the TEM-A heater foils in its outer hull to measure the thermal conductivity and the STATIL tiltmeter in its aft section)
3. Radiometer (RAD), which is mounted under the lander deck, albeit facing away from the area where HP^3 and SEIS are deployed (compare Fig. 11)
4. Back End Electronics (BEE), located in the lander warm electronics box

The Mole (see Sect. 3.3) has a length of 400 mm and together with the fully deployed science tether can reach a maximum depth of 5 m measured from its tip. Although reaching this depth will be the best compromise between the requirement of measuring the heat flow as quickly and as accurately as possible and the limits placed by planetary protection rules, a depth of 3 m will suffice to satisfy the mission science requirements. The temperature sensors on the science tether (compare Sect. 3.4) are unequally spaced to allow a better resolution of the undisturbed temperature gradient at depth.

A functional block diagram of the instrument package is shown in Fig. 3, where science sensors are indicated in yellow and the back-end electronics (BEE) package in blue. We will discuss the major hardware elements of HP^3 in the following starting with the BEE; the most important performance parameters are summarized in Table 1.

3.2 The HP^3 Backend Electronics

The HP^3 Backend Electronics (BEE) is accommodated in the lander's warm electronics box and controls all functions of the instrument. The BEE interfaces with the lander's telemetry and power system, but is designed to operate independently from the lander's main electronics, thus enabling data acquisition while the lander is in its power-saving sleep mode. Data is stored in the BEE's non-volatile memory and transmitted to the lander for downlink during lander wake-ups. The BEE controls the instrument's operation modes (compare Sect. 5), monitors instrument health, reads all science and housekeeping sensors, and operates the Mole launch lock, heaters, and the Mole motor. The BEE memory is dimensioned to be capable of keeping all mission data within itself. The only active electronics components apart from sensors outside the BEE are located in the radiometer sensor head, as analog to digital conversion of the small thermopile signals needs to be performed in close proximity to the sensors themselves.

To accurately measure subsurface temperatures, the TEM-P sensors on the science tether are measured using a 4-wire (Kelvin) configuration. Two 24-bit analog-to-digital converters (ADCs) within the BEE are used, with 8 differential input channels each. Seven of these channels per ADC are connected to PT100 sensors on the science tether while the remaining channel is connected to a highly stable 100 Ohm reference resistor. Connection of sensors, odd and even (compare Fig. 8), is alternating between the two ADCs to provide robustness against the failure of one complete ADC.

A constant current source supplies 0.5 mA and is connected to a demultiplexer, which switches the current between the PT100 sensors and the 100 Ohm reference resistor. A multiplexer inside the 24 bit ADC switches the PT100 signal to an instrument amplifier for

Table 1 Summary of major engineering budgets and key performance characteristics

Property		Value	Units
Mass	Support structure[a]	2085	g
	TLM	77	g
	Mole	860	g
	Science Tether	75	g
	Backend electronics	660	g
Size	Support structure[a]	$650 \times 418 \times 453$	mm^3
	TLM	$46 \times 51 \times 28$	mm^3
	Mole	$\varnothing 27 \times 400$	mm^3
	Science Tether	$4855 \times 36 \times 0.2$	mm^3
	Backend electronics	$200 \times 84 \times 150$	mm^3
Ops temperature	Support structure	153 to 323	K
	TLM	233 to 323	K
	Mole	228 to 323	K
	Science Tether	213 to 323	K
	Backend electronics	238 to 323	K
Non-Ops temperature	Support structure	153 to 323	K
	TLM	168 to 323	K
	Mole	168 to 323	K
	Science tether	153 to 323	K
	Backend electronics	238 to 323	K
Calibration temp. range	TEM-P	198 to 323	K
	TEM-A	198 to 323	K
Uncertainty[b]	TEM-P temp.	0.01	K
	TEM-P temp. diff.	0.0065	K
	TEM-A	0.05	K
	STATIL	1	°
	TLM	4	mm
	Conductivity	3.5	%
	Heat flow[c]	2.2	$mW\,m^{-2}$
Resolution	TEM-P	0.001	K
	TEM-A	0.0025	K
	STATIL	0.2	°
	TLM	4	mm
Hammering frequency[d]	Mole	0.28	Hz
Depth progress per stroke	Mole	0.1–1	mm
Energy consumption[e]	Hammering mode	47	Wh
	Cooldown mode	106	Wh
	Conductivity mode	142	Wh
	Monitoring mode	68	Wh
Measurement frequency	TEM	1/16	Hz
	STATIL	10	Hz

Table 1 (*Continued*)

Property		Value	Units
Data rate[f]	Conductivity mode	5.9	MBit/sol
	Monitoring mode	1.5	MBit/sol
Date volume[f]	Hammering mode	1.8	MBit

[a]Not including TLM, Mole, and Science Tether, but including mounting brackets and Engineering Tether

[b]Values given are 1-σ confidence limits

[c]For nominal operating conditions (cp. Section 4)

[d]Depth progress strongly depends on the unknown regolith resistance

[e]Including heating power under nominal operating conditions. Hammering time is 4 h. Cooldown, conductivity, and monitoring time is 24 h per sol

[f]Including housekeeping data. Hammering mode duration is 4 h

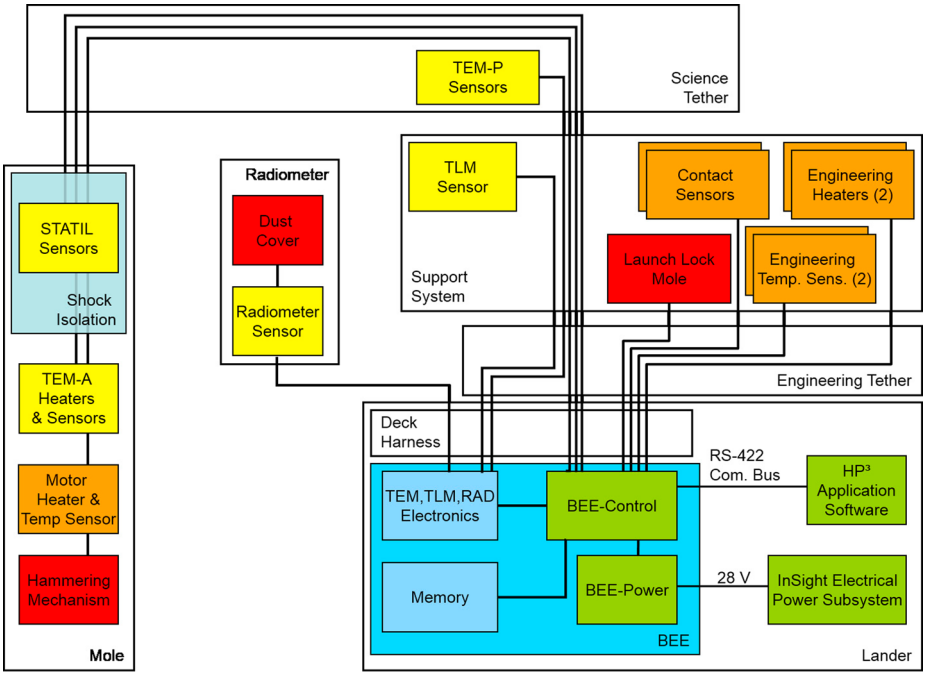

Fig. 3 Functional block diagram of the HP^3 instrument: Telemetry, power, and software interfaces in green, backend electronics hardware in blue, engineering heaters and sensors in orange, mechanisms in red, science sensors in yellow. The different functional sub-units (BEE, Deck Harness, Engineering Tether, Support Structure, Radiometer, Science Tether, Mole) are indicated by boxes

signal conditioning. The amplified analog signal voltage drop is then converted to a digital record inside the ADC. In addition, a reference offset measurement is taken with no current supplied to allow noise signals caused by, e.g., thermal voltages to be measured and subtracted. The reference voltage is supplied to both the ADC and the current source simul-

taneously. Any drift of the reference voltage can thereby be eliminated from the converted voltages, reducing measurement errors.

The ADC is operated at an oversampling rate of 4.8 kHz, and values are averaged in the FGPA to one sample. Typically, 600 samples are taken per channel, the first 88 of which are discarded to avoid transient effects after switching to another multiplexer channel. The 512 remaining samples are then again averaged to one value. Sampling all channels of the ADC then takes two seconds including the nominal and the offset voltages. Altogether, a measurement of the PT100 resistance consists of the following steps: First, the voltage drop across the PT100 is measured with and without current supplied. Then, the voltage drop across the reference resistor is measured in the same way. The resistance R_{PT} of the PT100 sensor is then given by

$$R_{\mathrm{PT}} = \frac{U_{\mathrm{PT}} - U_{\mathrm{PT},off}}{U_{Ref} - U_{Ref,off}} \cdot R_{Ref} \tag{4}$$

where the subscript *off* refers to the measurement without current supply, U_{ref} is the voltage drop across the reference resistor, and R_{Ref} is the resistance of the reference resistor. The measured PT100 resistance is then converted to temperature using the sensor's $R(T)$ calibration curve.

Thermal conductivity is measured by supplying a constant heating power to the TEM-A heater foils (see Sect. 3.4) and measuring the temperature rise of the heaters. The TEM-A circuitry in the BEE consists of two current sources and independent ADCs, which measure the voltage drop across the heater $U_{\mathrm{TEM\text{-}A}}$ as well as the voltage drop across a 10 Ohm shunt resistor U_{Shunt} in a 4-wire configuration. The current through the TEM-A heaters equals the current through the 10 Ohm shunt resistor and is given by

$$I_{\mathrm{TEM\text{-}A}} = \frac{U_{Shunt}}{10\ \Omega} \tag{5}$$

while the resistance of the TEM-A heating foils is given by

$$R_{\mathrm{TEM\text{-}A}} = \frac{U_{\mathrm{TEM\text{-}A}}}{I_{\mathrm{TEM\text{-}A}}} \tag{6}$$

Since copper heaters are used for TEM-A, the heaters simultaneously act as temperature sensors, and TEM-A resistance readings are converted to temperatures using the heater's $R(T)$ calibration curves. Heating power is then given by

$$Q(t) = I_{\mathrm{TEM\text{-}A}}(t)^2 R_{\mathrm{TEM\text{-}A}}(t) \tag{7}$$

for each of the TEM-A heating foils. Heating power is commandable between 0 and 1 W per heating foil, and power is held constant by a PID (proportional-integral-derivative) controller implemented in the BEE's field-programmable gate array (FPGA) such that $Q(t) = Q_0 = const$.

The STATIL subsystem uses two dual-axis accelerometers to determine the attitude of the HP^3 Mole with respect to the planetary gravity vector. The voltage signal output is digitized using the TEM-A ADCs, and the resulting reading is proportional to the angle of the tiltmeter's long axis with respect to gravity. TLM, the Tether Length Monitor, uses a four channel opto-electrical measurement to determine the length of extracted tether by reading a length code, which consists of a relative code equally spaced 2 mm apart and a 14 bit absolute code (see Fig. 7). When moving through the TLM, the tether coding dots

interrupt the illumination of the receiving photo transistor by the illuminating infrared LED. This analog signal is converted to a digital signal inside the BEE. The absolute code is based on a 7 bit Gray code counter, a 5 bit EDAC (error detection and correction) code and two synchronization bits. This results in a tether position synchronization interval of 56 mm.

The radiometer (RAD) electronics are located inside the radiometer sensor head but RAD has a digital and power interface to the BEE board. In addition, the BEE controls the RAD switch-on temperature via housekeeping sensors and engineering heaters. After switch-on, the temperature of the RAD sensor head is controlled by a PID controller inside the BEE's FPGA. The two RAD ADCs within the sensor head measure 3 sensors in one field of view (FOV) each. Thermopile signals of the three filters in each FOV are fed to the ADC via a low pass input filter. The thermopile voltage is converted to a surface brightness temperature using the thermopile calibration curves. PT100 sensors inside the thermopile sensors measure the cold-junction temperatures. PT100 are supplied with a current limited by a 47 kOhm resistor, resulting in a permanent current of 50 μ A, small enough to eliminate self-heating effects. A FET can switch the measurement ground (GND) of all PT100 sensors, which is used to measure voltage offsets for the PT100 lines. A low drift 100 Ohm reference resistor is measured in the same configuration as the PT100 sensors for each ADC and PT100 readings are referenced to this resistor. This eliminates drift of the reference voltage.

A measurement of a PT100 channel resistance takes the four steps described above for the PT100 sensors on the science tether and the resistance of a PT100 sensor is calculated from Eq. (4).

3.3 The HP^3 Mole

The HP^3 Mole is a small, low velocity penetrator working as a self-impelling nail powered by a hammering mechanism in its interior. The hammer mass is accelerated by a spring and impacts periodically on an anvil connected to the Mole's hull, thereby driving the Mole forward. The recoil is in part absorbed by friction on the hull and in part by a brake spring. The distribution of masses in the mechanism and the anisotropic friction of the regolith on the Mole cause the hammering mechanism to function as a mechanical diode directing the Mole preferentially in the forward direction. The first Mole has been developed by VINit Transmash in Russia and was described by Gromov et al. (1997). It has been further developed at DLR (e.g., Richter et al. 2004) as a sampling tool for the ill-fated Beagle II lander on MarsExpress and for potential heat flow probes on missions such as ExoMars and Bepi-Colombo (Spohn et al. 2001). A second line of Mole development was achieved more or less in parallel at CBK, Warsaw (e.g., Grygorczuk et al. 2011; Seweryn et al. 2014) who have also constructed a Mole based on an electromagnetic hammering system similar to the hammering mechanism of the MUPUS penetrator flown on the Rosetta mission (e.g., Grygorczuk et al. 2007; Spohn et al. 2007). The present HP^3 Mole is a further development of the DLR Mole but with a hammer mechanism from CBK and Astronika, Warsaw.

Figure 4 shows the interior of the HP^3 Mole. From left to right, there is a multi-purpose backcap (MPC) which serves as the mechanical interface where the science tether enters the Mole interior and as the launch-lock interface. Further to the right is the payload cage that contains STATIL and the shock isolation springs to protect the STATIL sensors from hammer shocks. The payload cage connects to the brake spring and a helical cable that routes electrical lines further down. The suppressor—termed for its mass which is significantly larger than the hammer mass—contains the DC motor, gearbox, and drive train to operate the hammer. The drive train connects to the hammer (made of tungsten) via a cylindrical cam and roller and the hammer is attached to the force spring. The inner surface of the tip

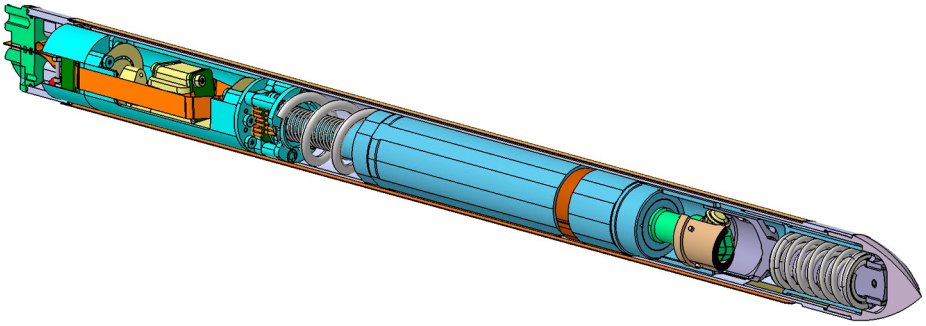

Fig. 4 CAD model showing (from left to right) the multi-purpose backcap (light green) with the feedthrough for the science tether, the payload cage (turquoise) with STATIL (yellow and orange) and the shock absorption springs, the brake spring assembly (grey) with the helical cable running to the motor, the suppressor (blue) with the DC motor, gearbox and drive train, the drive shaft (green) and cam and roller (brown), the hammer (dark violet), the force spring (grey), and the Mole tip (violet). The latter has an ogive outer shape optimized to reduce the resistance of the regolith against forward motion

(made of titanium) provides the anvil against which the hammer is driven. Note that the suppressor casing extends towards the tip, encasing the cam and part of the hammer. On moving forward the suppressor casing can hit onto a notch on the inner surface of the tip to provide a second stroke, in addition to the hammer stroke as will be described in the following.

Figure 5 illustrates the hammering cycles and the working principle of the Mole. The main masses are color coded in the figure indicating the hammer (green), the suppressor (blue) and the outer hull (grey). In addition, the payload cage and STATIL are shown in yellow and pink, respectively. The DC-motor, turning continuously, drives the cylindrical cam that pulls the hammer away from the tip, compressing the force spring. After the maximum pull is reached (Fig. 5, top frame), the force spring and the hammer are both released together due to a gap in the cylindrical cam and the hammer is accelerated forward towards the tip (Fig. 5 frame 2). The suppressor—suspended from the brake spring—is accelerated backwards (Fig. 5 frame 2–5) at the same time. Since the suppressor mass is 4.4 times the hammer mass, most of the force spring energy is transferred to the hammer's kinetic energy. The hammer separates from the spring after it is fully relaxed and continues to move freely before it impacts on the tip anvil for the first major stroke (Fig. 5 frame 2–3).

After the break spring has reached its maximum compression (Fig. 5 frame 5), the suppressor mass is accelerated towards the tip (Fig. 5 frame 6–7) driven by gravity and the relaxing brake spring. Finally, the suppressor casing impacts the tip for a second major stroke to cause additional forward motion of the outer hull (Fig. 5 frame 7). Due to rebounds of the parts, a few additional but much less energetic strokes can occur subsequently but these are too weak to provide further advancement in the regolith and the mechanism comes to rest (frame 7). A full cycle has an average duration of 3.7 to 3.8 s depending on ambient conditions. Lichtenheldt et al. (2014) give a detailed analysis of the cycle including an analysis of elastic waves propagating from the Mole and related effects.

The Mole has been operated and tested in various test stands at atmospheric pressure and temperature as well as under simulated martian conditions. In addition, the Mole has undergone the usual testing for space hardware including functional, vibrational and thermal/vacuum testing (see Table 1 for allowable flight temperatures). Test stands used include devices where the Mole is fixed vertically and hammering against a spring, to devices simulating low gravity and allowing the strength of the Mole stroke to be quantified. A deep

Fig. 5 Phases of a hammering cycle (top to bottom, cf. Lichtenheldt et al. (2014)) showing the interaction between the hammer (green), the suppressor (blue), and the outer hull (grey). (1) Mechanism fully tensioned. (2) The hammer is released and impacts the tip, providing the first stroke. (3) Recoil movement of the suppressor, compressing the brake spring. (4) Recoil movement of hammer and suppressor away from the tip. (5) Suppressor point of reversal is reached. (6) and (7) The brake spring and gravity drive hammer and suppressor tipwards, providing a second stroke. (8) Mechanism at rest

penetration testbed was used in Bremen at DLR that allowed for penetrating into various test sands up to 5 m but at ambient temperature and pressure. This test bed is shown in Fig. 6 and has an inner diameter of about 0.8 m.

A similar testbed but capable of achieving Mars subsurface conditions of 213 K and martian atmospheric composition and pressure was used at JPL. The vacuum chamber contains regolith simulant to a depth of 2 m and the maximum depth of burial for the Mole was 1.7 m. That test bed was also used for a successful full functional test of the HP^3 system. Other test stands included vacuum chambers at ZARM in Bremen with about a meter of sand and with adjustable ambient pressure. The main regolith simulants for these tests were a nearly cohesionless quartz sand (WF-34), Mojave Mars simulant (MMS, <2 mm size fraction), and a sand/dust mixture consisting of mechanically crushed commercially available basalt (see Vrettos et al. 2014 and Delage et al. 2017 for details about the test sands). Geological analysis of the landing site identified the quartz sand as the most realistic regolith simulant with respect to particle size, particle size distribution, and particle shape; and thus the emergent properties of cohesion, angle of repose, and absolute and relative density. Figure 6 right shows deep penetration test results for various Mole hardware models. In the WF-34 simulant, the Mole was always able to reach the minimum tip-depth of 3 m within 21 hours of continuous operation.

The dynamic behavior of the Mole is highly complex with the rate of progress depending on the soil mechanical properties such as compaction, friction angle and density. These will depend on the preparation of the soil and the environmental conditions at the test stand. Moreover, due to the high shock loads and the operation inside of the soil, the working of the

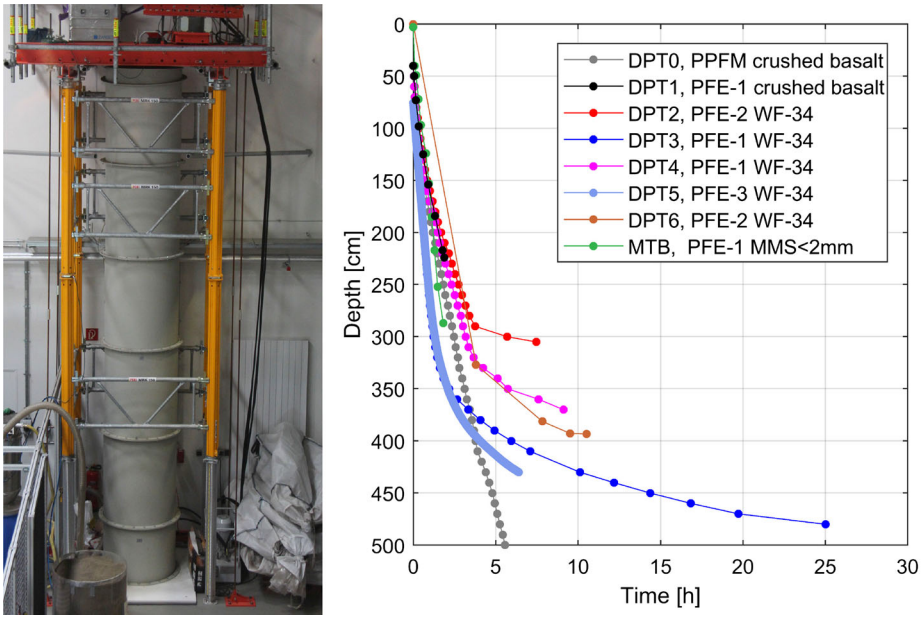

Fig. 6 5.5 m deep penetration testbed (left) and depth to the tip of the Mole over time (right)

hammer mechanism in the soil is not directly observable, although X-rays (both still images and high-speed video) and magnetic resonance imaging have been used to control proper alignment of interior parts. The working of the Mole mechanism has also been studied in a transparent housing. To be able to predict the effects of design changes as well as to analyze the dynamic behavior, simulation models have been used throughout the whole design process (Lichtenheldt and Schäfer 2013; Lichtenheldt et al. 2014; Lichtenheldt 2015; Lichtenheldt and Krömer 2016) resulting in significant optimizations of the Mole performance.

3.4 The HP^3 Thermal Sensors TEM-P and TEM-A

HP^3 measures the subsurface temperature gradient using industry standard thin-film platinum sensors with a nominal resistance of 100 Ohm at 273.15 K (PT100) mounted on the science tether (TEM-P). Sensors are connected to the electronics using a 4-wire configuration and the mounting of a representative temperature sensor is shown in Fig. 7. The copper cross-section inside the science tether is minimized such that heat shunting along the tether is negligible, and PT100 sensor lines have a cross section of 200 × 17 µm. The total copper cross section inside the tether is 0.3 mm^2, including the wider current carrying heater lines (400 µm) and Mole motor lines (800 µm). The spacing between sensors increases with greater distance from the Mole backend along the science tether to allow a denser spacing at depths where the amplitude of the annual temperature wave is comparatively small (compare Fig. 8). The sensors near the surface will be used to measure the daily and annual thermal wave. Analysis of the attenuation of the annual wave as a function of depth will be used to determine the thermal diffusivity of the regolith.

HP^3 measures thermal conductivity by using the Mole as a modified line-heat source via the TEM-A heater foils embedded in the Mole's casing. This approach consists of injecting a known amount of heat into the probe and measuring the probe's self-heating curve. For a

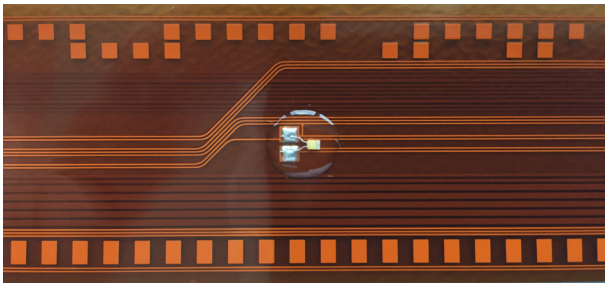

Fig. 7 Segment of the prototype science tether with sensor #12 in the center. The sensor is located to the right of two solder points. The sensor and the solder points are covered with a circular silicon coating. Also visible are lines to the sensor and to deeper sensors and the Mole. At the top, the Gray code markings for the absolute TLM depth measurements are shown. The regular spaced markings at the bottom provide higher-resolution relative position data

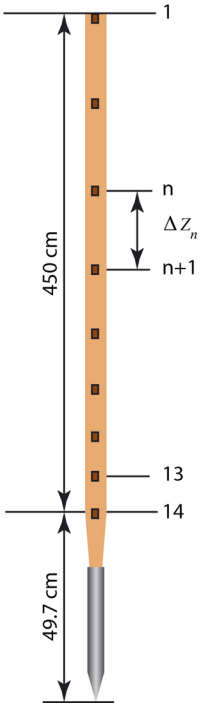

Number	Depth [cm]	Spacing [cm]
1	0.003	
		46
2	0.463	
		44
3	0.913	
		42
4	1.333	
		40
5	1.733	
		38
6	2.123	
		37
7	2.483	
		35
8	2.833	
		33
9	3.163	
		31
10	3.463	
		29
11	3.753	
		27
12	4.023	
		25
13	4.273	
		23
14	4.503	

Fig. 8 Arrangement of sensors on the tether (left) and distances to depth and between sensors. Sensors are more densely spaced towards the Mole to allow a better depth resolution of the temperature gradient

finite length cylinder such as the Mole, the heating curve for $t \to \infty$ takes the form (Grott et al. 2010)

$$\Delta T = C_1 \ln(t) + C_2 \tag{8}$$

where t is time, and the constant C_1 is primarily a function of heating power and regolith thermal conductivity, while C_2 is a function of the probe's heat capacity and the contact conductance between probe and regolith. Therefore, thermal conductivity can be determined

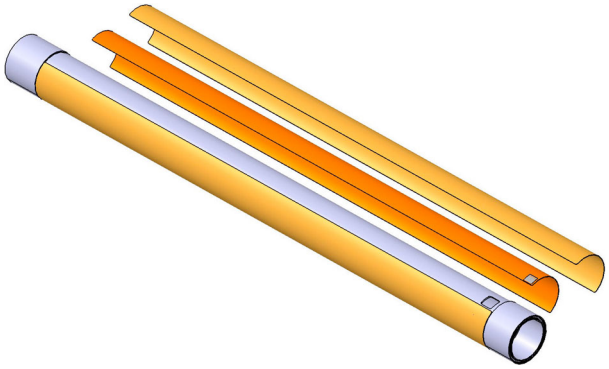

Fig. 9 Half-exploded view of the mounting of the TEM-A heating foils (orange) on the Mole outer hull (gray). To protect the heating foils from abrasion during Mole hammering, foils are covered by aluminum half shells (gold). Heaterfoil cables are routed through two windows inside the Mole outer hull (bottom right)

from

$$C_1(k, Q) = \frac{\partial \Delta T}{\partial \ln(t)} \tag{9}$$

Analytical solutions for $C_1(k, Q)$ exist for ideal line heat sources (Carslaw and Jaeger 1959) and for sensors with finite heat capacity and large length to diameter ratios (Jaeger 1956). We use a numerical thermal model of the Mole and its environment to determine the temperature increase of the casing as a function of time for a given heating power Q. Thermal conductivity k is then obtained by a fit of the numerical model to $\partial \Delta T / \partial \ln(t)$ (e.g., Langseth et al. 1972; Grott et al. 2010), and parameters necessary for setting up the numerical model will be published together with the HP^3 calibration report.

The TEM-A heaters are Kapton-based copper heaters glued to the outer casing of the Mole and protected against abrasion by aluminum covers (Fig. 9). Due to the large temperature coefficient-of-resistance of copper, the heaters simultaneously act as temperature sensors. The TEM-A electronics inside the BEE measures the heating power Q (between 0 and 2 W) as well as the resistance of the heaters to determine the self-heating curve as a function of time for a given heater power.

3.5 The HP^3 Depth Determination

To monitor where the temperature and thermal conductivity measurements are taken, HP^3 includes two sensors to measure the length of science tether pulled out of the support structure and the tilt of the Mole body with respect to gravity. The reconstruction of the Mole path and the depth of the temperature sensors rests on the assumption supported by tests that the tether follows the path where the Mole has been and does not migrate through the regolith as more tether is pulled into the ground. The length of paid-out tether and the Mole attitude with respect to gravity, both of which are monitored continuously as the Mole is penetrating, can be combined to determine the depth beneath the surface of the Mole and the sensors embedded in the science tether. The Mole attitude is measured by the STATIL tiltmeter located in the payload cage of the Mole (compare Fig. 4). The STATIL tiltmeter consists of two accelerometers mounted at a known, fixed angle to each other on two printed circuit boards (PCBs) (Fig. 10). The latter are attached to a sled made of stainless steel. The sled is fixed to two double shock mitigation springs, to avoid high shock loads at the sensors due to the hammering. The sled is mounted such that its longitudinal axis coincides with the longitudinal axis of the Mole (compare Fig. 4). The electrical signal from the PCBs is fed through the science tether and the engineering tether to the BEE (compare Fig. 3).

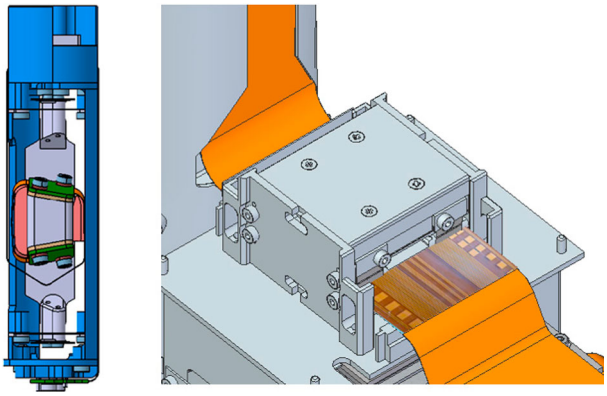

Fig. 10 Left: CAD model of the payload cage inside the Mole housing the tiltmeter (STATIL). Electronics are protected from shocks by two sets of springs towards the top and the bottom of the assembly, visible as horizontal thin black lines, and the tiltmeter accelerometers are mounted at an angle with respect to the Mole axis on the printed circuit boards (green). The reddish blocks are flex-cable guides. Right: CAD model of the tether length monitor (TLM) mounted on the support structure. The science tether (orange) is fed through the detector, absolute depth encoding is located on the right-hand-side in this perspective, and relative depth encoding is on the left-hand-side

The length of extracted tether is determined by optical sampling of position codes on the science tether by the tether length measurement system (TLM). A CAD drawing of the TLM is shown in Fig. 10. The tether encodes distance using opaque copper coding dots that are 2 mm long with 2 mm spacing. As seen in Fig. 7, one side of the tether encodes relative distance using regularly spaced dots, while the opposite side of the tether encodes absolute length using a Gray-code with 14 bits per datum (code length $= 14 \times 4$ mm). TLM works in a transmitted-light mode; the trace of code dots is illuminated inside the TLM by two pairs (one main and one redundant on each side of the tether) of 880 nm light emitting diodes. A phototransistor opposite each LED detects the opaque and transparent segments and delivers a digital signal (light/no light) to the BEE. The phototransistor signal is amplified by an operational amplifier with input hysteresis to reduce jitter and signal ringing.

The relative and absolute position decoding is done in the BEE's digital field programmable gate array (FPGA) logic. Absolute length along the tether is obtained by multiplying the absolute distance code by 14 times 4 mm (the length of an absolute coding byte), and the relative distance code is updated accordingly. The relative distance code is incremented by 4 mm every time a new relative code is read, until 14 bits have again been collected and a new absolute code is available. In this way, intermittent data loss can be recovered by reading a new absolute code. The BEE can detect non-valid data (due, for example, to single-bit errors) and can correct the absolute distance counter. If more than one bit is rejected by the BEE (e.g., a two-bit error in the data), the presently-read absolute value cannot be reconstructed and the absolute measure is rejected. The relative counter keeps incrementing, updating the temporary count since the last valid absolute measurement. Once the next valid absolute value code is read, both relative and absolute TLM counters are updated.

TLM can only detect changes at the code track due to tether movement; it is not possible to capture the current position in a static configuration. The first measurements taken by TLM after being switched on increments the relative distance counter until 14 bits have been processed and a new absolute code mark is available. The depth to the Mole tip is

obtained by adding an offset, which contains both the distance between the TLM sensor and the martian surface and the distance from the Mole tip to the first code on the tether. Thus, the tip-of-the-Mole-depth below the surface of Mars is given by

$$l = (N_{abs} \cdot 14 + \Delta N_{rel} + \mathrm{TLM}_{off}) \cdot 4 \,(\mathrm{mm}) \tag{10}$$

where the offset is given in units of the coding pitch (4 mm), N_{abs} is the absolute counter, and ΔN_{rel} is the number of relative codes read since the last absolute code. The TLM offset is 87 units for the TLM main sensors and 93 units for the redundant sensors. In the raw data, conversion to absolute depth is automatically done in the instrument's FPGA, including switching between main and redundant sensors and offsets if needed.

3.6 The HP^3 Radiometer

The HP^3 radiometer (RAD) is mounted underneath the lander deck with its line-of-sight pointing approximately 180° away from where the HP^3 SSA will be located. We expect that the terrain North of the lander will be similar to the terrain to the South, where we deploy our instruments. This is supported by geological context images from orbit. The RAD is thus pointed to a representative patch of regolith that is guaranteed not to have the instruments placed in it. More specifically, in the nominal case of landing on flat ground with the solar panel oriented East-West, the radiometer will observe the surface at azimuth 20° West (counting azimuth counter-clockwise starting from north), with boresight elevations of −55° and −25° relative to the horizon. The radiometer has two sets of thermopile sensors, consisting of three sensors each, defining two fields of view to provide a more representative measurement of the surface brightness temperature. The approximate location of the radiometer FOVs relative to the lander are shown in Fig. 11.

During the northern winter it is likely that the solar panel shadows will pass through the closer FOV in the morning and in the afternoon, thus providing an estimate of the effect of the shadow on the surface temperature forcing. Nominally the shadow of the Eastern solar panel will pass through shortly after sunrise, and the shadow of the western panel around 2–3 pm local time. Depending on the actual orientation of the lander, the footprint geometry, and the surface properties, several tens of K difference are expected between the two FOVs if one of them will be in shadow. However, for supporting the interpretation of the subsurface temperatures determined by TEM-P, average daily surface temperatures need to be known. Hourly measurements of surface temperature planned for at least every 30 sols will resolve the diurnal curve including the effects of shadow. Thermal modelling fitting this diurnal curve will allow transient shadows to be eliminated form the analysis. The shadow trajectories change with the season so that the closer FOV will not experience any shadow over half of the year. The more distant FOV is mostly unaffected by shadows even if there were some lander tilt. In case of extreme lander tilts of 12 deg (likelihood of 1%) both FOVs might be affected by shadow from the lander. The difference in temperature between the two FOVs during the periods of no shadow will help constrain the effect of thermal emission from the lander.

The radiometer measures surface brightness temperatures using IPHT TS 72 thermopile sensors. A sensor consists of an IR filter and an absorber of $D = 0.5$ mm dimension in radiative equilibrium with the target surface in the sensor's field of view. The temperature of the absorber is determined using $Bi_{0.87}Sb_{0.13}$/Sb (Bismuth-Antimony) thermopairs with an electro-motive force of EMF = 135 μV/K. The thermal voltage generated by the temperature difference between the junctions of the thermocouples is a measure of the net radiative

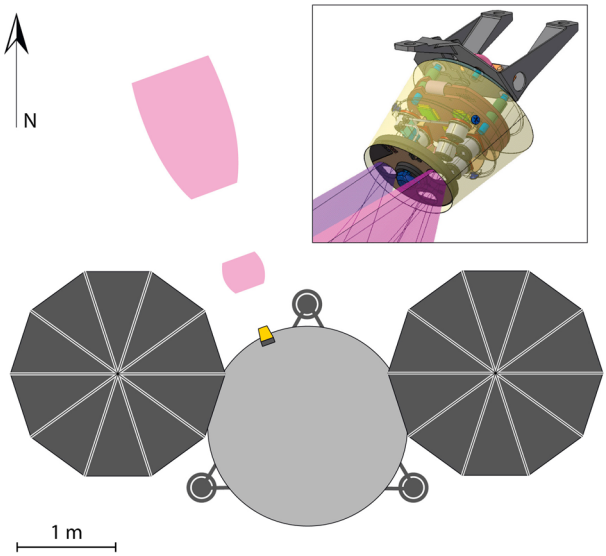

Fig. 11 Insert: Semi-transparent CAD model of the radiometer (RAD) showing the two sets of three thermopile sensors (grey cylinders with black top surface) together with their respective cones of view (violet). The dust cover actuator is located in the middle of the sensor head. Main panel: The two fields of view of RAD are marked in violet and are shown relative to the lander. RAD is mounted below the lander deck facing away from the area where SEIS and the HP^3 SSA are deployed (bottom of the image, south on Mars) to avoid disturbance of the measurement by the deployed InSight instruments. The solar panels of the lander are shown along with the three feet. The lander deck is indicated by markings representing hardware located on the deck

flux between the absorber and the target. The thermal voltage is given by

$$U_{th} = SA_d\pi\nu \int_{\lambda_1}^{\lambda_2} \tau(\lambda)\big(\epsilon B_\lambda(T) - B_\lambda(T_{ref})\big)\, d\lambda + \nu_H \int_0^{\infty} \big(\epsilon_H B_\lambda(T_H) - B_\lambda(T_{ref})\big)\, d\lambda \tag{11}$$

where S is the sensor sensitivity (in V/W), A_d is the absorber area (in m^2), ϵ is the target surface emissivity, ν is the target's view factor, τ is the sensor transmissivity, B is the Planck-function, T is the surface temperature, T_{ref} is the temperature of the sensor's cold junction serving as reference, T_H is the sensor housing temperature, ϵ_H is the emissivity of the sensor housing, and ν_H is the view factor of the sensor housing. To eliminate the second term in the equation, the sensor head temperature is stabilized such that $T_H = T_{ref}$. The spectral transmittance of the filters is shown in Fig. 12. PT100 sensors mounted inside the sensor housing measure the cold junction temperature. Therefore, a total of 12 signals are recorded: 6 thermopile voltages corresponding to 3 bandpass filters in two fields of view each, and 6 corresponding cold-junction temperatures measured by PT100 sensors.

The fields of view are geometrically limited by the sensorhead apertures to 20° degrees (full-width, half-maximum). In addition to that, a calibration target obscures a part of this 20° deg circular FOV. Its temperature provides part of the thermopile signal and is measured by another PT100 sensor. The radiometer performance parameters are summarized in Table 2.

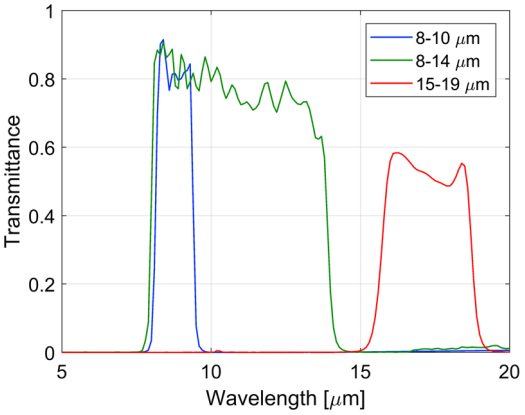

Fig. 12 Spectral transmittance of the radiometer filters. Two of the filters, 8–14 μm and 15–19 μm, are the same as in the REMS GTS radiometer on the Mars Science Laboratory (Gómez-Elvira et al. 2012). The broad bandpass (8–14 μm) is the primary filter for measuring brightness temperatures while the two other filters add the capability of resolving an inhomogeneous temperature distribution in the field of view by spectral deconvolution. Inhomogeneities could result from rocks, shadows, or pockets of very fine dust with high thermal inertia

4 Heat Flow Error Budget

As discussed in Sect. 2.3, a measurement of the planetary heat flow F requires independent measurements of the regolith thermal conductivity k as well as the thermal gradient $\partial T/\partial z$, and we will rewrite Eq. (2) according to

$$F = k\frac{\partial T}{\partial z} = k\frac{\theta}{L} \tag{12}$$

for the following discussion.

The thermal gradient is determined from a measurement of the temperature difference between different sensors θ as outlined in Sect. 3.4, and the vertical separation L between sensors is determined using the STATIL tiltmeter and the tether length monitor TLM as discussed in Sect. 3.5.

Thermal conductivity is determined by providing a known power to the probe and measuring the sensor's self heating curve as discussed in Sect. 3.4, and thermal conductivity is then given by

$$k = \frac{q}{4\pi m C_1} \tag{13}$$

where q is the heating power per unit length supplied to the Mole. The HP^3 backend electronics measures the sourced current I using 10 Ohm shunt resistors (Sect. 3.2), and the resistance of the heating foils R is determined by measuring the voltage drop across the heaters. Heating power per unit length is then given by

$$q = \frac{\mathrm{RI}^2}{l_{Mole}} \tag{14}$$

Table 2 Radiometer overview giving the major engineering budgets as well as the key performance characteristics

Property		Value	Units
Mass	Sensor head	106	g
Size	Sensor head	95 × 58 × 72	mm^3
Ops temperature	Sensor head	233 to 323	K
Non-Ops temperature	Sensor head	163 to 323	K
Spectral range	Thermopiles	8–14, 8–10, 15–19	µm
Field of view	Full-width, half-maximum	20	°
Incidence angle[a]	FoV-1	65	°
	FoV-2	35	°
Calibration temp. range	Thermopiles	170 to 300	K
Calibration setpoints	Sensor head	238, 268, and 298	K
Uncertainty[b]	at $T > 170$ K, 8–14 µm	2	K
	at $T > 210$ K, 8–10 µm	4	K
	at $T > 210$ K, 15–19 µm	4	K
Noise	Electronics	20	nV
	Thermal	100	nV
NETD[c]	8–14 µm at 170 K	0.1	K
	8–10 µm at 170 K	0.6	K
	15–19 µm at 170 K	0.7	K
Energy consumption[d]	Standard mode	77	Wh
	Hourly mode	136	Wh
	Calibration mode	15	Wh
Measurement frequency	All modes	1/15	Hz
Data rate[e]	Standard mode	0.1	MBit/sol
	Hourly mode	0.4	MBit/sol
Data volume[e]	Calibration mode	0.5	MBit

[a]For nominal landing conditions and a non-tilted lander

[b]Values given are 1-σ confidence limits as determined during calibration by verification measurements. These estimates do not include long-term drift of the sensors or mounting induced heater offsets. These will be accounted for by inflight calibration

[c]NETD: Noise Equivalent Temperature Difference

[d]Including heating power under nominal operating conditions. Standard and hourly modes executes 4 and 24 measurements per sol, respectively. Calibration mode duration is 2 h 40 min

[e]Not including housekeeping data. Calibration mode duration is 2 h 40 min

where l_{Mole} is the length of the Mole. Finally, the logarithmic temperature rise m of the probe at large times t is given by

$$m = \frac{dT}{C_1\, d(\ln(t))} \tag{15}$$

where the scaling factor C_1 is given by Eq. (9). The measurement induced heat flow uncertainty is then given by a Gaussian propagation of individual uncertainty contributions,

Table 3 Estimated contributions to the heat flow error budget assuming a nominal regolith thermal conductivity of 0.05 W m^{-1} K^{-1} and a surface heat flow at the landing site of 20 mW m^{-2}. Estimates are given for a final Mole-tip depth of 3 m, and all numbers represent 1-σ confidence limits

Error source	Term	Error
Slope uncertainty TEM-A	$\Delta\, m/m$	2.5%
Heat input uncertainty TEM-A	$\Delta q/q$	0.1%
Temperature difference uncertainty	$\Delta\theta/\theta$	0.5%
Depth difference uncertainty	$\Delta L/L$	1.0%
Uncertainty in thermal conductivity	$\Delta F/F_{cond}$	2.6%
Uncertainty in temperature gradient	$\Delta F/F_{grad}$	1.2%
Uncertainty in the annually averaged temperature	$\Delta F/F_{avg}$	10%
Total		10.8%
Total [mW m^{-2}]		2.2

and

$$\left(\frac{\Delta F}{F}\right)_{meas} = \sqrt{\left(\frac{\Delta m}{m}\right)^2 + \left(\frac{\Delta q}{q}\right)^2 + \left(\frac{\Delta\theta}{\theta}\right)^2 + \left(\frac{\Delta L}{L}\right)^2} \tag{16}$$

However, additional systematic sources of uncertainty need to be taken into account. First of all, depending on regolith thermal conductivity and the achieved final depth, the annual temperature wave may not have completely decayed at the emplacement depths of the relevant sensors. Therefore, measurements need to be conducted over an extended period of time, ideally covering a full martian year (Grott et al. 2007). Due to the constraints imposed by the mission, only part of the annual wave may be sampled, as part of the primary mission, and some modeling uncertainties remain. This error has been estimated using Monte-Carlo simulations of the inversion, taking random instrument errors into account. The contribution was found to be 2 mW m^{-2}, 1 mW m^{-2}, and 0.5 mW m^{-2} if measurements are extended over 0.6, 0.25, and 0.1 martian years for final Mole tip depths of 3 m, 4 m, and 5 m, respectively.

Furthermore, the heat injected into the regolith by the HP^3 experiment during penetration disturbs the thermal state of the regolith. This perturbs the thermal conductivity and thermal gradient measurements, and while the operational profile is optimized to minimize these effects (Sect. 5), the total time available for regolith re-equilibration is limited by the need to sample the annual temperature wave. Therefore, two additional terms accounting for the conductivity and gradient errors need to be included in the error budget. Gaussian error propagation for these errors then results in the final error budget

$$\left(\frac{\Delta F}{F}\right)_{tot} = \sqrt{\left(\frac{\Delta F}{F}\right)^2_{meas} + \left(\frac{\Delta F}{F}\right)^2_{cond} + \left(\frac{\Delta F}{F}\right)^2_{grad} + \left(\frac{\Delta F}{F}\right)^2_{avg}} \tag{17}$$

where the last three terms refer to the uncertainty in the conductivity, in the gradient, and in the determination of the average temperature from the sampling of the annual wave, respectively.

The different contributions to the total error budget are summarized in Table 3, and estimates assume a nominal regolith thermal conductivity of 0.05 W m^{-1} K^{-1} as well as a surface heat flow of 20 mW m^{-2} at the landing site. The assumed depth to the Mole tip

is the minimum depth of 3 m. As is evident from the table, the term dominating the error budget is the error in determining the average annual temperature at each sensor, which results from the relatively large amplitudes of the annual temperature wave at shallow depth. This error is considerably reduced if sensors are emplaced to greater depths, where the annual wave naturally attenuates, and this uncertainty contribution roughly halves per meter of additional depth beyond 3 m. Overall, a 1-σ heat flow uncertainty of 2.2 m W m^{-2} can be achieved in the nominal case for a final Mole tip depth of 3 m and observing for 0.6 martian years. In the worst case of low thermal conductivity and high heat flow, the total heat flow error is 4.5 mW m^{-2} under the same observing conditions. The expected total error will be about 1 mW m^{-2} or 5% if the target depth of 5 m will be reached.

5 Instrument Operations

The HP^3 instrument will be deployed onto the surface of Mars by InSight's robotic arm, and the general geometry of potential placement sites is given in Fig. 13. InSight will land in an east-west orientation, putting the workspace for instrument deployment to the south of the lander. It is desired to place HP^3 as far away from the lander and the SEIS instrument as possible, but this will need to be weighed against any rocks or surface irregularities that would affect deployment of HP^3 or SEIS.

After deployment of the instrument onto the surface of Mars by the InSight robotic arm, operation of the HP^3 instrument is split into two main phases, the penetration phase and the monitoring phase. During the penetration phase, the HP^3 Mole will advance into the subsurface, trailing behind the science tether equipped with temperature sensors (TEM-P) to measure the thermal gradient. The first hammering phase (compare Fig. 14) will be initiated around 50 sols after landing and will be stopped at a depth of 70 cm. Both the heat generated within the Mole and the heat deposited in the regolith during penetration will then be allowed to dissipate for a period of at least 2 sols. A TEM-A measurement will be executed thereafter to determine the thermal conductivity of the regolith. Heating times for the TEM-A measurement will be 24 h and the heating will be adjusted to allow a TEM-A temperature rise of 10 K, sufficiently large for a good signal-to-noise ratio without significantly affecting the regolith thermal conductivity. At this point in time, a ground-in-the-loop phase is foreseen. Data from TEM-A will be evaluated on the ground before deciding to resume hammering. This will allow a re-run of the conductivity experiment with different TEM-A heating power settings if needed. Hammering will be then be resumed until the next stop is reached at 30 cm further down and the cooldown phase and the thermal conductivity measurement will be repeated. No ground-in-the-loop phase is foreseen here because the thermal conductivity is expected to only slowly vary with depth. A maximum of eight additional stops at depth intervals of 50 cm are foreseen to reach the target depth of 5 m and to compile a depth profile of thermal conductivity underneath the landing site. Progress of the Mole is continuously monitored by STATIL and the TLM. Their data will allow to uniquely determine the Mole depth, from which the depth of individual temperature sensors can be derived.

After reaching the final depth, HP^3 will enter the monitoring phase. The final depth is limited to 5 m by planetary protection rules and, therefore, by the designed-in maximum length of the science tether, but may be shallower depending on the performance of the Mole. During the monitoring phase, the TEM-P sensors will regularly take temperature measurements. Readings will be taken for 5 min every hour; these values will be averaged to yield an hourly sampling of the subsurface temperature up to the end of mission.

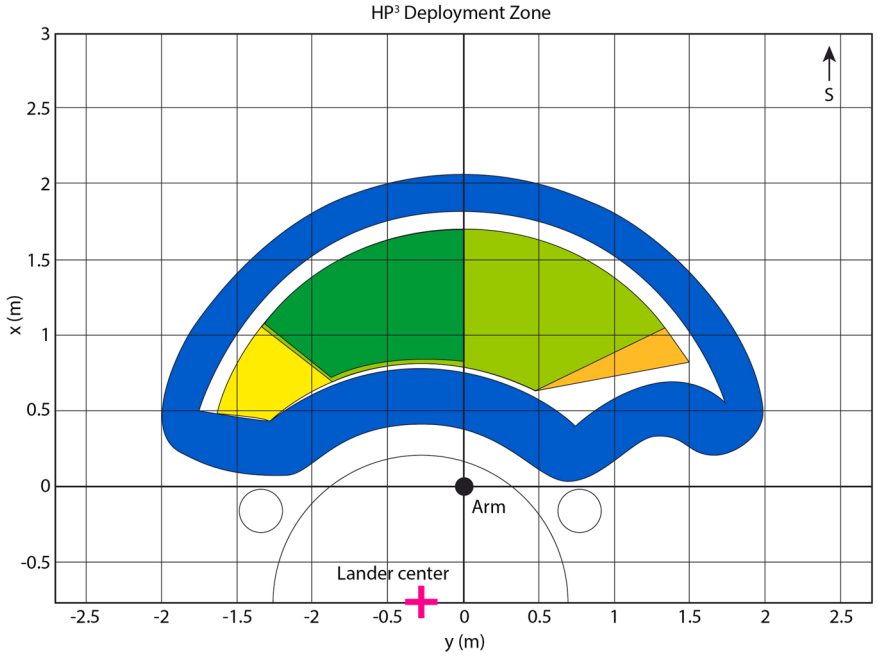

Fig. 13 Map of the HP^3 deployment zone defined by the reach of the robotic arm for placing HP^3 onto the martian surface. (South is pointing to the top of the figure.) The lander, its geometrical center, and the shoulder of the arm are schematically shown in the lower part of the figure. Distances are measured from the shoulder of the arm. The thick blue line envelopes the possible placement sites for the SSA feet. The green, yellow, and orange areas indicate the nominal, less preferred, and unfavored locations of the center of mass of the HP^3 instrument, respectively. The dark green area marks the preferred locations within the nominal area. Less preferred and unfavored locations are either too close to the lander with unwanted shadowing or would force the Engineering Tether to cross the SEIS tether. It would also be comparatively difficult to image the instrument with the lander cameras, there

A single radiometer measurement starts with commanding the heating of the radiometer sensor head to one of its operational setpoints (compare Table 2) and the sensor head is then left to thermally equilibrate for 1 hour. Subsequently, 20 samples of the thermopile and PT100 sensors are acquired over 5 minutes if the default operating parameters are used. The timing of telecommand execution, the sampling rate (up to 0.5 Hz), equilibration duration, and measurement duration are adjustable to allow for flexible observations of occasional events that are expected to occur at certain times of the day, such as eclipses and shadows moving into the FOV.

The radiometer operation modes, which determine the timing of measurements and the temperature of the sensor head, consist of multiple measurements in a predefined order. The radiometer standard mode includes 4 measurements per sol at around 2 am, 5 am, 2 pm and 5 pm local time. This mode is run continuously unless there is a switch to another mode or unless the radiometer has to remain off due to power/energy constraints. The radiometer hourly mode acquires 24 measurements per sol. This mode is intended to be executed every 30 sols. If sufficient energy is available, the hourly mode will be executed more frequently.

Because the sensor head is only passively cooled, the radiometer temperature must be above the ambient temperature to allow efficient cooling to the environment. The radiometer temperature control is adjusted to the diurnal cycle to reduce energy consumption as well

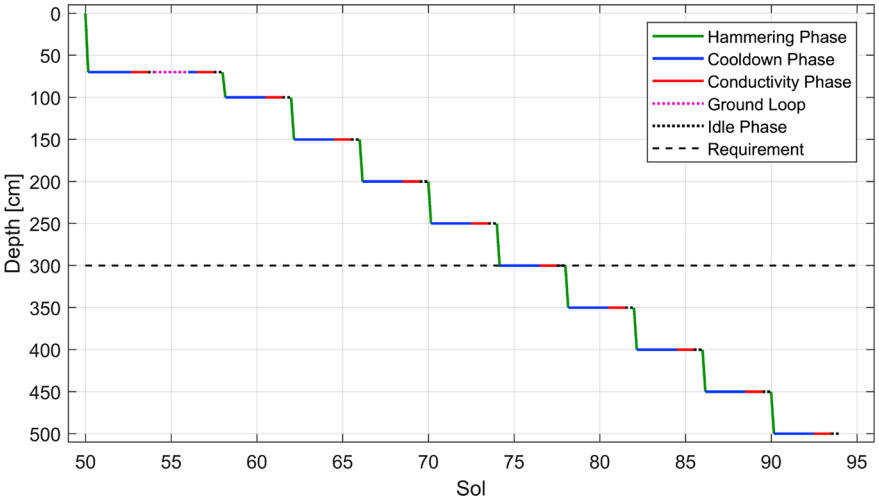

Fig. 14 Schematic depth vs. time diagram showing the planned HP^3 penetration operations. Mole release is foreseen to occur around sol 50 after landing. The Mole then hammers until its tip has reached a depth of 70 cm, followed by at least two sols of Mole and regolith cooldown to equilibrate subsurface temperatures with the surroundings. A one-sol thermal conductivity experiment follows, before the instrument switches to idle mode. Data from TEM-A will be evaluated prior to proceeding to the next depth (ground-in-the-loop) allowing for a re-run of the conductivity experiment with different TEM-A heating power settings if needed. Hammering is then resumed until a depth of 1 m is reached where the cooldown and the thermal conductivity measurement are repeated. A maximum of additional eight such cycles of hammering, cooling and thermal conductivity measurement will be executed but with depth intervals of 50 cm

as measurement uncertainty and the operation modes switch between the night time observation setpoint ($T_{night} = 238$ K) and the day time setpoint ($T_{day} = 268$ K) at approximately 9 am local time. A third setpoint ($T_{hot} = 298$ K) can be commanded manually if necessary.

In the radiometer standard and hourly modes, the temperature of the dust cover (acting as a calibration target) is stabilized at the same temperature as the sensorhead body, but during the calibration mode the dust cover temperature is varied relative to the sensorhead. Since part of the dust cover remains in the instrument's field of view after the cover is opened, a defined signal is generated that can be used to (re)calibrate the sensors over a limited temperature range in flight.

6 Summary and Conclusions

The Heat Flow and Physical Properties Package HP^3 has been designed and built to satisfy the InSight mission science requirements, in particular to determine the local surface heat flow to an uncertainty of ± 5 mW m^{-2}. The success of the instrument package will depend to a significant extent on the largely unknown thermal and mechanical regolith properties at the InSight landing site. The InSight geology working group have meticulously explored these properties to the extent possible using available remote sensing data of the landing area and in-situ data from previous landing sites (Golombek et al. 2017). Nevertheless, there remains some uncertainty in the conduciveness of the bulk regolith to Mole digging, and the probability of encountering a buried Mole-blocking rock. Thermal properties, specifically conductivity, govern the depth of the annual disturbance of the subsurface temperature field

and the temperature gradient to be measured from which the heat flow will be derived. The magnitude and speed of propagation of disturbances to the subsurface temperature field from landing (albedo change due to dust blowoff) and due to lander shadows will depend on the conductivity. In general, a small (but still measurable) conductivity will result in slower disturbance propagation and larger thermal gradients for HP^3 to measure.

With the surface heat flow—albeit measured at one location only (but see Plesa et al. 2016a)—planetary scientists will get an important quantity characteristic of the whole planet not directly measured before. With the surface heat flow the composition of the planet can be better constrained, possibly even helping to discriminate between competing cosmochemical models. For the modelers of the interior dynamics and evolution of the planet including magnetic field generation, the surface heat flow value will provide an invaluable constraint.

But the expected scientific harvest of the HP^3 package goes further. Never before on Mars and on any other terrestrial planet or moon have near surface layers been explored to a comparable depth *in-situ* and temperature and thermal conductivity been measured. Data from the Mole progress will be available to constrain mechanical properties of the regolith such as density, cohesion, angle of internal friction and grain size distribution by analytical (e.g., Hansen-Goos et al. 2014) and numerical modeling (e.g., Lichtenheldt 2015; Lichtenheldt and Krömer 2016; Marshall et al. 2017; Poganski et al. 2017; Golombek et al. 2018).

Should HP^3 be successful, similar instruments can be designed and built for future missions. Depending on the regolith properties, solutions like HP^3 reaching meter depths or MUPUS-like solutions (e.g., Grygorczuk et al. 2007; Spohn et al. 2007) for depths of 10s of centimeters appear to be feasible. Possible targets include the Moon and Phobos. At icy satellites, combinations of hammering mechanisms and melting probes (e.g., Dachwald et al. 2014) are possible.

Acknowledgements The design, building of and research into the HP^3 has been supported by the German Aerospace Center DLR, by NASA, the ÖAW, and the Polish Academy of Science. This paper is InSight Contribution Number 41.

References

R.A. Albert, R.J. Phillips, Geophys. Res. Lett. **27**, 2385 (2000)
G.R. Beardsmore, J.P. Cull, *Crustal Heat Flow* (Cambridge University Press, Cambridge, 2001)
M. Beuthe, S. Le Maistre, P. Rosenblatt et al., J. Geophys. Res. (2012). https://doi.org/10.1029/2011JE003976
D. Breuer, W.B. Moore, in *Treatise on Geophysics*, vol. 10, ed. by T. Spohn, G. Schubert 2nd edn. (Elsevier, New York, 2015), p. 255
D. Breuer, T. Spohn, Geophys. Res. Lett. **20**, 1655 (1993)
C.D. Brown, R.J. Phillips, J. Geophys. Res. **105**, 13221 (2000)
E.C. Bullard, Proc. R. Soc. Lond. Ser. A **173**, 474 (1939)
E.C. Bullard, Ocean Proc. R. Soc. Lond. Ser. A **222**, 408 (1954)
H.S. Carslaw, J.C. Jaeger, *Conduction of Heat in Solids*, 2nd edn. (Clarendon, Oxford, 1959)
B. Dachwald, J. Mikucki, S. Tulaczyk, I. Digel, Ann. Glaciol. (2014). https://doi.org/10.3189/2014AoG65A004
I.J. Daubar, A.S. McEwen, M.P. Golombek, *46th Lunar Planet. Sci. Conf., Abstract* (2015), p. 2225
V. Dehant, B.W. Banerdt, P. Lognonné et al., Planet. Space Sci. (2012). https://doi.org/10.1016/j.pss.2011.10.016
P. Delage, E. Karakostas, M. Belmokthar, P. Lognonné et al., Space Sci. Rev. (2017). https://doi.org/10.1007/s11214-017-0339-7

A.A. Fraeman, J. Korenaga, Icarus **210**, 43 (2010)
P.E. Geissler, R. Sullivan, M. Golombek, J.R. Johnson, K. Herkenhoff, N. Bridges, A. Vaughan, J. Maki, T. Parker, J. Bel, J. Geophys. Res. **115**, E00F11 (2010)
M.P. Golombek, L.S. Crumpler, J.A. Grant et al., J. Geophys. Res. (2006). https://doi.org/10.1029/2005JE002503
M.P. Golombek, A.F.C. Haldemann, R.A. Simpson, R.L. Fergason, N.E. Putzig et al., in *The Martian Surface: Composition, Mineralogy and Physical Properties*, ed. by J.F. Bell III. (Cambridge University Press, Cambridge, 2008), p. 468
M.P. Golombek, N. Warner, C. Schwartz, J. Green, in *Lunar Planet. Sci. Conf., XLIV, Abstract 1696* (2013)
M.P. Golombek, D. Kipp, N. Warner, I.J. Daubar et al., Space Sci. Rev. (2017). https://doi.org/10.1007/s11214-016-0321-9
M.P. Golombek, M. Grott, G. Kargl et al., Space Sci. Rev. (2018). https://doi.org/10.1007/s11214-018-0512-7
J. Gómez-Elvira, C. Armiens, L. Castañer et al., Space Sci. Rev. (2012). https://doi.org/10.1007/s11214-012-9921-1
R. Greeley, P.D. Spudis, Rev. Geophys. (1981). https://doi.org/10.1029/RG019i001p00013
V.V. Gromov, A.V. Miskevich, E.N. Yudkin et al., *Proc. 7th Europ. Space Mech. Trib. Symp.* (ESTEC, Noordwijk, 1997)
M. Grott, Planet. Space Sci. **57**, 71 (2009)
M. Grott, E. Hauber, S.C. Werner et al., Geophys. Res. Lett. **32**, L21201 (2005)
M. Grott, J. Helbert, R. Nadalini, J. Geophys. Res. **112**, E09004 (2007)
M. Grott, J. Knollenberg, C. Krause, J. Geophys. Res. **115**, E11005 (2010)
J. Grygorczuk, M. Banaskiewicz, K. Seweryn, T. Spohn, J. Telecommun. Inf. Technol. **1**, 50 (2007)
J. Grygorczuk, M. Banaskiewicz, A. Chichocki et al., *Proc. ASTRA Conf.* (ESTEC, Noorwijk, 2011)
T. Guillot, D. Gautier, in *Treatise on Geophysics*, ed. by T. Spohn, G. Schubert 2nd edn. (Elsevier, New York, 2015). https://doi.org/10.1016/B978-0-444-53802-4.00176-7
C. Güttler, I. von Borstel, R. Schräpler, J. Blum, Phys. Rev. E (2013). https://doi.org/10.1103/PhysRevE.87.044201
A. Hagermann, Philos. Trans. R. Soc. A **363**, 2777 (2005)
B.C. Hahn, S.M. McLennan, E.C. Klein, Geophys. Res. Lett. **38**, L14203 (2011)
U. Hammerschmidt, W. Sabuga, Int. J. Thermophys. **21**, 217 (2000a)
U. Hammerschmidt, W. Sabuga, Int. J. Thermophys. **21**, 1225 (2000b)
H. Hansen-Goos, M. Grott, R. Lichtenheldt, C. Krause et al., *45th Lunar Planet. Sci. Conf., Abstract* (2014), p. 1325
E. Hauber, M. Grott, P. Kronberg, Earth Planet. Sci. Lett. **294**, 393 (2010)
E. Hauber, P. Brož, F. Jagert et al., Geophys. Res. Lett. **38**, L10201 (2011)
S.A. Hauck, R.J. Phillips, J. Geophys. Res. **107**, 5052 (2002)
J.W. Head, J.F. Mustard, M.A. Kreslavsky et al., Nature **426**, 797 (2003)
G. Heiken, D. Vaniman, B. French (eds.), *Lunar Sourcebook* (Cambridge University Press, Cambridge, 1991)
J. Helbert, D. Reiss, E. Hauber, J. Benkhoff, Geophys. Res. Lett. **32**, L17201 (2005)
J. Helbert, G. Arnold, J. Benkhoff et al., Adv. Space Res. (2006). https://doi.org/10.1016/j.asr.2005.05.007
A.W. Hofmann, in *Treatise on Geochemistry*, ed. by H.D. Holland, K.K. Turekian 2nd edn. (Elsevier, New York, 2014). https://doi.org/10.1016/B978-0-08-095975-7.00203-5
E.S. Hütter, N.I. Kömle, G. Kargl, E. Kaufmann, J. Geophys. Res. (2008). https://doi.org/10.1029/2008JE003085
J.C. Jaeger, Aust. J. Phys. (1956). https://doi.org/10.1071/PH560167
C. Jaupart, J.C. Mareschal, in *Treatise on Geophysics*, ed. by T. Spohn, G. Schubert 2nd edn. (Elsevier, New York, 2015). https://doi.org/10.1016/B978-0-444-53802-4.00114-7
W.S. Kiefer, Planet. Space Sci. (2012). https://doi.org/10.1016/j.pss.2011.07.016
W.S. Kiefer, Q. Li, Geophys. Res. Lett. **36**, L18203 (2009)
M.A. Kreslavsky, J.W. Head III., Geophys. Res. Lett. (2002). https://doi.org/10.1029/2002GL015392
P. Kronberg, E. Hauber, M. Grott et al., J. Geophys. Res. **112**, E04005 (2007)
M.G. Langseth, S.P. Clark, J.L. Chute et al., *Earth Moon Planets* (1972). https://doi.org/10.1007/BF00562006
M.G. Langseth, S.J. Keihm, K. Peters, *Proc. Lunar Sci. Conf.*, vol. 7 (1976), p. 3143
J. Laskar, A.C.M. Correia, M. Gastineau et al., Icarus **170**, 343 (2004)
M.T. Lemmon, M.J. Wolff, J.F. Bell III. et al., Icarus (2015). https://doi.org/10.1016/j.icarus.2014.03.029
R. Lichtenheldt. *IFToMM D-A-CH* (2015). ISBN 978-3-940402-03-5
R. Lichtenheldt, O. Krömer, in *Earth and Space 2016: Engineering for Extreme Environments*, ed. by R.B. Malla, J.H. Agui, P.J. van Susante (ASCE Library, Reston, 2016), p. 142
R. Lichtenheldt, B. Schäfer, in *10. Kolloquium Getriebetechnik*, ed. by L. Zentner (Universitätsverlag Ilmenau, Ilmenau, 2013), p. 169

R. Lichtenheldt, B. Schäfer, O. Krömer, T. van Zoest, in *3rd International Conference on Multibody System Dynamics*, ed. by K. Sung-Soo, C.J. Hwan (2014). ISBN 978-89-950027-7-3
K. Lodders, B. Fegley, Icarus (1997). https://doi.org/10.1006/icar.1996.5653
P. Lognonné, W.B. Banerdt, D. Giardini et al., Space Sci. Rev. (2018, this issue)
R.D. Lorenz, Icarus **250**, 262 (2015)
J.P. Marshall, T.L. Hudson, J.E. Andrade, Space Sci. Rev. (2017). https://doi.org/10.1007/s11214-016-0329-1
P.J. McGovern, S.C. Solomon, D.E. Smith et al., J. Geophys. Res. **107**, E12 (2002)
P.J. McGovern, S.C. Solomon, D.E. Smith et al., J. Geophys. Res. **109**, E07007 (2004)
M.T. Mellon, B.M. Jakosky, Geophys. Res. Lett. **19**, 2393 (1992)
M.T. Mellon, B.M. Jakosky, H.H. Kieffer, P.R. Christensen, Icarus (2000). https://doi.org/10.1006/icar.2000.6503
J.W. Morgan, E. Anders, Geochim. Cosmochim. Acta (1979). https://doi.org/10.1016/0016-7037(79)90180-7
P. Morgan, M. Grott, M. Golombek, P. Delage, Space Sci. Rev., (2018, this issue)
A. Morschhauser, M. Grott, D. Breuer, Icarus **212**, 541 (2011)
J.F. Mustard, C.D. Cooper, M.K. Rifkin, Nature **412**, 411 (2001)
S. Nagihara, M. Hedlaund, K. Zacny, Planet. Space Sci. **92**, 49 (2014)
T. Nakagawa, P.J. Tackley, Earth Planet. Sci. Lett. **329**, 1 (2012)
G. Neukum, R. Jaumann, H. Hoffmann et al., Nature **432**, 971 (2004)
G.A. Neumann, M.T. Zuber, M.A. Wieczorek et al., J. Geophys. Res. **109**, E08002 (2004)
R.J. Phillips, M.T. Zuber, S.E. Smrekar et al., Science (2008). https://doi.org/10.1126/science.1157546
S. Piqueux, P.R. Christensen, J. Geophys. Res. **114**, E09005 (2009a)
S. Piqueux, P.R. Christensen, J. Geophys. Res. **114**, E09006 (2009b)
A.C. Plesa, N. Tosi, M. Grott et al., J. Geophys. Res. **120**, 995 (2015)
A.-C. Plesa, M. Grott, M. Lemmon et al., J. Geophys. Res. (2016b). https://doi.org/10.1002/2016JE005127
A.-C. Plesa, M. Grott, N. Tosi et al., J. Geophys. Res. (2016a). https://doi.org/10.1002/2016JE005126
J. Poganski, N.I. Kömle, G. Kargl et al., Space Sci. Rev. (2017). https://doi.org/10.1007/s11214-016-0302-z
H.N. Pollack, S.J. Hurter, J.R. Johnson, Rev. Geophys. **31**(3), 267–280 (1993)
M.A. Presley, P.R. Christensen, J. Geophys. Res. **102**, 9221 (1997)
M.A. Presley, R.A. Craddock, J. Geophys. Res. (2006). https://doi.org/10.1029/2006JE002706. 2006
L. Richter, P. Coste, V.V. Gromov, A. Greszik, *Proc. 8th ESA Workshop Adv. Space Tech. Rob. and Autom.* (ESTEC, Noordwijk, 2004), I-11–I-14
S.W. Ruff, P.R. Christensen, D.L. Blaney et al., J. Geophys. Res. **111**, E12S18 (2006)
J. Ruiz, C. Fernández, D. Gomez-Ortiz et al., Earth Planet. Sci. Lett. **270**, 1–12 (2009)
R.A. Schultz, T.R. Watters, Geophys. Res. Lett. **28**, 4659 (2001)
K. Seweryn, J. Grygorczuk, R. Wawrzaszek et al., Acta Astron. (2014). https://doi.org/10.1016/j.actaastro.2014.03.004
M.A. Siegler, S.E. Smrekar, J. Geophys. Res. **119**, 47 (2014)
M.A. Siegler, S.E. Smrekar, S. Piqueux et al., Space Sci. Rev. **211**, 259 (2017)
J.R. Spencer, J.A. Rathbun, L.D. Travis et al., Science (2000). https://doi.org/10.1126/science.288.5469.1198
T. Spohn, in *Treatise on Geophysics*, vol. 10, ed. by T. Spohn, G. Schubert 2nd edn. (Elsevier, New York, 2015), p. 1
T. Spohn, F. Sohl, D. Breuer, Astron. Astrophys. Rev. **8**, 181 (1998)
T. Spohn, A. Ball, K. Seiferlin et al., Planet. Space Sci. **49**, 1571 (2001)
T. Spohn, K. Seiferlin, A. Hagermann et al., Space Sci. Rev. (2007). https://doi.org/10.1007/s11214-006-9081-2
D.J. Stevenson, T. Spohn, G. Schubert, Icarus **54**, 466 (1983)
S. Taylor, *Planetary Crusts: Their Composition, Origin and Evolution* (Cambridge University Press, Cambridge, 2008). https://doi.org/10.1017/CBO9780511575358
G.J. Taylor, W. Boynton, J. Brückner et al., J. Geophys. Res. **111**, E03S10 (2006a)
G.J. Taylor, W. Boynton, J. Brückner et al., J. Geophys. Res. **111**, E03S06 (2006b)
A.H. Treiman, M.J. Drake, M.-J. Janssens et al., Geochim. Cosmochim. Acta **50**, 1071 (1986)
J. Vaucher, D. Baratoux, N. Mangold et al., Icarus **204**, 418 (2009b)
J. Vaucher, D. Baratoux, M.J. Toplis et al., Icarus **200**, 39 (2009a)
C. Vrettos, A. Becker, K. Merz, L. Witte, in *Earth & Space 2014: Engineering for Extreme Environments*, ed. by L.S. Gertsch, R.B. Malla (ASCE Library, Reston, 2014), p. 10
H. Wänke, G. Dreibus, Philos. Trans. R. Soc. Lond. A **349**, 285 (1994)
N.H. Warner, M.P. Golombeck, J. Sweeney et al., Space Sci. Rev. (2017). https://doi.org/10.1007/s11214-017-0352-x
M.A. Wieczorek, M.T. Zuber, J. Geophys. Res. **109**, E01009 (2004)
A.S. Yen, R. Gellert, C. Schröder et al., Nature (2005). https://doi.org/10.1038/nature03637
M.T. Zuber, S.C. Solomon, R.J. Phillips et al., Science **287**, 1788 (2000)